Kobe University Repository : Thesis

学位論文題目 Title	Research on ion implantation damage of the materials for the next generation semiconductor device(次世代半導体材料のイオン注入損傷に関する研究)
氏名 Author	Shibata, Satoshi
専攻分野 Degree	博士（工学）
学位授与の日付 Date of Degree	2011-03-25
資源タイプ Resource Type	Thesis or Dissertation / 学位論文
報告番号 Report Number	甲5305
権利 Rights	
URL	http://www.lib.kobe-u.ac.jp/handle_kernel/D1005305

※当コンテンツは神戸大学の学術成果です。無断複製・不正使用等を禁じます。著作権法で認められている範囲内で、適切にご利用ください。

Create Date: 2017-12-19

Doctoral Dissertation

Research on ion implantation damage of the materials for the next generation semiconductor device.

（次世代半導体材料のイオン注入損傷に関する研究）

January 2011

Graduate School of Maritime Sciences, Kobe University

Satoshi Shibata

CHAPTER 1. GENERAL INTRODUCTION - 3 -

1.1. RESEARCH BACKGROUND - 3 -

1.2. ION IMPLANTATION MACHINES USED FOR SEMICONDUCTORS - 4 -

1.2.1. THE SITUATION OF STATE OF THE ART ION IMPLANTATION MACHINES. - 5 -

1.2.2. THE ROLE OF ION IMPLANTATION IN FABRICATION PROCESS OF CMOS DEVICES - 8 -

1.2.3. THE ROLE OF ION IMPLANTATION IN FABRICATION PROCESS OF CCD IMAGE SENSORS - 12 -

1.2.4. MEASUREMENT TECHNOLOGY - 14 -

1.3. SIGNIFICANCE AND PURPOSE OF THE PRESENT STUDY - 15 -

1.4. STRUCTURE OF THE DISSERTATION - 17 -

CHAPTER 2. EVALUATION OF PRE-AMORPHIZED LAYER THICKNESS AND INTERFACE QUALITY OF HIGH-DOSE SHALLOW IMPLANTED SILICON BY SPECTROSCOPIC ELLIPSOMETRY - 20 -

2.1. INTRODUCTION - 20 -

2.2. EXPERIMENTAL DETAILS - 21 -

2.2.1. SAMPLE PREPARATION - 21 -

2.2.2. THICKNESS MEASUREMENT TECHNIQUE - 22 -

2.3. RESULT AND DISCUSSION - 23 -

2.3.1. AMORPHIZED LAYER THICKNESS - 23 -

2.3.2. DISCUSSIONS - 30 -

2.3.3. ROUGHNESS EVALUATION OF AMORPHOUS/CRYSTALLINE INTERFACE BY SE - 32 -

2.4. APPLICATIONS - 36 -

2.4.1. PRE-AMORPHIZATION BY GE AND AS ION IMPLANTATION - 37 -

2.4.2. AMORPHIZATION BY HE RF PLASMA DOPING - 39 -

2.5. CONCLUSION - 40 -

CHAPTER 3. NEW EVALUATION METHOD FOR CROSS-CONTAMINATION OF ION IMPLANTATION BY USING GRAZING ANGLE INCIDENCE PIXE IN PHOTO-RESIST - 41 -

3.1. INTRODUCTION - 41 -

3.2. EXPERIMENTAL PROCEDURE - 43 -

3.2.1. SAMPLE PREPARATION - 43 -

3.3.2. EXPERIMENTAL APPARATUS - 44 -

3.3. RESULTS AND DISCUSSION .... - 44 -

3.3.1. PIXE ANALYSIS WITH LARGE TILT ANGLE .... - 44 -

3.3.2. REDUCTION OF BREMSSTRAHLUNG BACKGROUND BY USING PHOTO-RESIST AS AN ALTERNATIVE LOW-Z SURFACE FOR ANALYSIS .... - 48 -

3.3.3. EVALUATION OF CROSS CONTAMINATION .... - 53 -

3.4. CONCLUSION .... - 55 -

CHAPTER 4. CHARGING PHENOMENA DURING MEDIUM CURRENT ION IMPLANTATION OF CARBONIZED PHOTO-RESIST SURFACE LAYERS .... - 57 -

4.1. INTRODUCTION .... - 57 -

4.2. EXPERIMENTAL PROCEDURE .... - 59 -

4.3. RESULTS AND DISCUSSIONS .... - 60 -

4.3.1. RELATIONS BETWEEN CARBONIZED LAYER AND IMPLANTED IMPURITIES .... - 60 -

4.3.2. THICKNESS OF CARBONIZED LAYER .... - 63 -

4.3.3. MECHANISM OF THE CARBONIZED LAYER FORMATION .... - 67 -

4.3.4. SURFACE POTENTIAL OF THE WAFER AND DISCHARGE .... - 69 -

4.3.5 CONSEQUENCES OF THE CHARGING PHENOMENA IN ACTUAL DEVICES .... - 73 -

4.4. CONCLUSION .... - 78 -

CHAPTER 5. CONCLUSION .... - 80 -

ACKNOWLEDGMENTS .... - 84 -

REFERENCES .... - 86 -

LIST OF PUBLICATIONS .... - 94 -

Chapter 1. General Introduction

1.1. Research Background

To cope with the drastic change of digitization and networking in today's world, the silicon-based semiconductor industry has made rapid developments, especially in miniaturization. As of 2010, the 32-nm gate-length node transistor is in mass production, and the 22-nm node transistor is also said to be in the final stages of development towards mass production. Moreover, for the system LSI (Large Scale Integration devices), with many functions integrated onto a single chip to achieve high efficiency and low cost consumer electronics, there has been an ever-increasing need for greater multi-functionality and higher performance, in addition to the miniaturization and high integration which was previously driven by memory requirements. At the same time, with the spread of digital steel cameras (DSC) and mobile phones which incorporate cameras, image sensors have started to take a share of the leading silicon-based semiconductor products.

As these cutting-edge devices have started to be manufactured, the major problem of "production tolerance" has come to the fore in recent years [1]. Amongst these, control over any variation in the characteristics of semiconductor components like transistors is important for regular production of goods.

The ion implantation technology which was invented by William Bradford Shockley Jr. et al., and then commercialized by Peter H. Rose et al., is the most accurate technique for doping a silicon substrate with impurities [2, 3]. The ion implantation technology and the subsequent evolution of annealing technology suppressed variation in the characteristics, and was a great factor in realizing regular production of minute

and high-performance Si-based semiconductors [4].

The degree of control required for the ion implantation machines for cutting-edge devices, as evaluated by the one-σ value divided by the mean value, is less than 1% both for the cross-wafer uniformity and the implantation repeatability, even for a 300mm wafer. To achieve this degree of control, not only the ion implantation machine itself, but the physical changes in the semiconductor material irradiated by the ions must also be accurately controlled. Most of these problems are hardly considered at the laboratory level, but arise as prominent issues for mass production facilities in manufacturing factories. Consequently, there is now a need for detection technology for these phenomena on the production line (in-line).

1.2. Ion Implantation Machines Used for Semiconductors

Figure 1 is a schematic diagram showing the parametric regions for the ion implantation that is used for manufacturing current Si semiconductor products such as Complementary Metal Oxide Semiconductors (CMOS) and Charge Coupled Device Image Sensors (CCD). Ion implantation has been used over a wide range of doses of 1×10^{11} cm^{-2} to 1×10^{17} cm^{-2}, and energies of 200eV to 8 MeV. Three kinds of the ion implantation machine have mainly been used in the production line to cover the wide ranges. These are (a) the high-current ion implantation machine to cover the high-dose (more than 1×10^{14} cm^{-2} with a beam current from 1 mA to 20 mA) and low-energy region (below 50 keV) with comparatively less implantation accuracy requirement, such as one to form the source/drain region, (b) the high-energy implantation machine to cover the high-energy region (above 200 keV), and (c) the medium-current ion implantation machine for the other parameter regions with high implantation accuracy.

The end-stations of the ion implantation machines are categorized into two kinds; the batch-type for which productivity is important, and the serial-type for which implantation accuracy is emphasized.

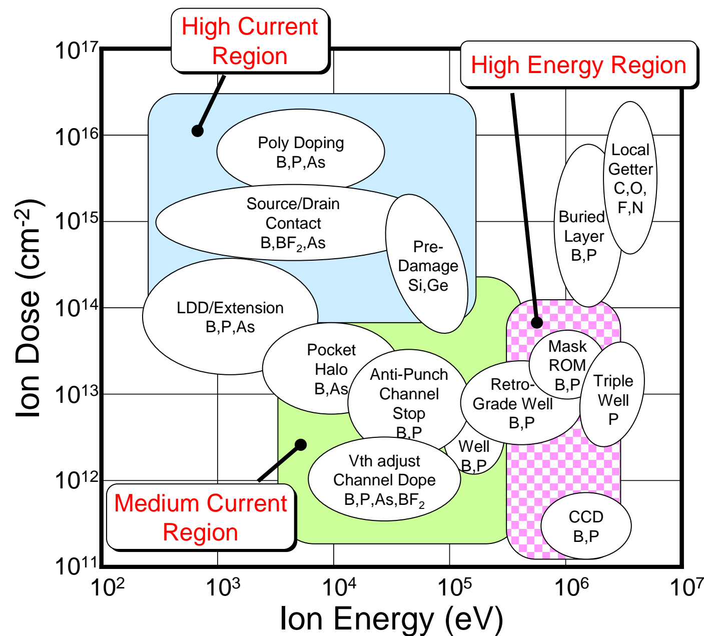

Fig.1-1. Parametric diagram showing ion implantation region used for semiconductor

1.2.1. The situation of state of the Art Ion Implantation Machines.

(a) High-current Ion Implantation Machines

This is an apparatus to provide ion implantation, e.g., for the CMOS source-drain, with doses of more than 1×10^{15} cm^{-2} and high currents of more than 10 mA. In general, the batch-type end-station has been adopted in order to boost productivity. The batch-type system can implant ions uniformly over the whole wafer surface by loading 10 wafers identically onto a disc, and rotating the loaded disc at speeds up to 1200 rpm while scanning the entire surface. However, since the beam scanning has not been applied to the high-current batch-type machines, it was possible to design the beam line fairly short. For this reason, it was relatively easy to design a low energy mashine, and

it was possible to ensure a few mA for beams with energies of smaller than 1 keV. It is thought that this has contributed greatly to the development of the shallow junction formation. On the other hand, however, implantation of positively-charged ions into the semiconductor material with a high beam current, has caused many problems due to accumulation of charge. To alleviate these problems, an electron gun was developed to actively supply negative charge to the surface of the wafer during ion implantation. This has become a standard equipment to be furnished in the high current implantation systems.

The wafers are held during disc rotation with the help of the centrifugal force without using cramps or something like that in order to avoid metal contamination, cross-contamination, etc. For this purpose the wafer holder is cone-shaped with a cone angle of the order of 1 ~ 5 degrees with respect to the beam axis. This introduces a systematic error in the incident angle of the ions within the range of the cone angle difference. As the miniaturization of the CMOS proceeds in recent years, problems have started to occur, such as asymmetry in the transistor characteristics [5] and "pattern toppling" [6]. The former is caused by the "shadowing" due to the tilt. The latter is the mechanical collapse of the minute gate electrode pattern on the Si surface due to the centrifugal force resulting from the high speed rotation, which causes a severe reduction in yield of the end product. This is why even high-current machines have started to use the serial-type instead of the batch-type recently [7, 8].

(b) Medium-current Ion Implantation Machines

The medium-current ion implantation machine is an apparatus developed to make an implantation with a controlled concentration in the channel part of the MOS device to the 1×10^{16} cm^{-2} range with high accuracy. The energy and the dose are in the ranges

of 5 ~ 200 keV (singly charged ions) and 1×10^{11} cm^{-2} to 1×10^{14} cm^{-2}, respectively. To meet the strong demand from device miniaturization, it has a mechanism to make the beam parallel using electric and magnetic fields, and/or a serial-type end station, so that the incident angle accuracy of 0.5 degrees or less is realized even over the whole surface of a 300-mm wafer.

Most serial-type systems adopt the hybrid scan mechanism which employs both the beam scan and the mechanical scan. In the latter scanning method the wafer holding stage (platen) are moved vertically relative to the ion beam. The beam current is monitored by a Faraday cup at the same position as the wafer during implantation, and the current fluctuation is minimized by immediate feedback to the scanning system. An extremely high doping accuracy is thus achieved with a dose inhomogeneity of less than 0.5 % and a reproducibility with inaccuracy of less than 0.5% [9, 10]. For complex device structures the step implantation mechanism has also been adopted to achieve high accuracy [11]. To incorporate multiple transistors on a single chip necessitated by the system LSI in recent years, there is an increasing need for employing the medium-current machine in multiple processes.

(c) High-energy Implantation Machines

High-energy implantation machines are mainly used in the process to form the well in MOS devices and the photodiode in CCD image sensors. In most cases implanters of heavy ions with 3-MeV energy range are used. Recently, however, to respond to the demand for increasingly high sensitivity for CCD devices in addition to miniaturization, ultra-high energy machines with maximum energies of 5 MeV for B^{3+}, 8 MeV for P^{4+} and 8 MeV for As^{4+} have been introduced into the market [13]. The maximum energy for B^{3+} ions is determined so as to avoid neutron production by the nuclear reaction with

deuterium atoms in the photo-resist, $D(^{11}B, n)^{12}C$ [12]. The maximum energies for other heavy ions are determined so that they have almost the same density profile.

Since the implantation depth in the Si substrate is several μm, the implantation accuracy has been the problem of secondary importance. In recent years, however, attempts to control the impurity depth profile [14] by making use of axial channeling in the Si substrate have been made, and the trend towards serial processing to meet the demands for the miniaturization of CCD devices [15] is becoming marked.

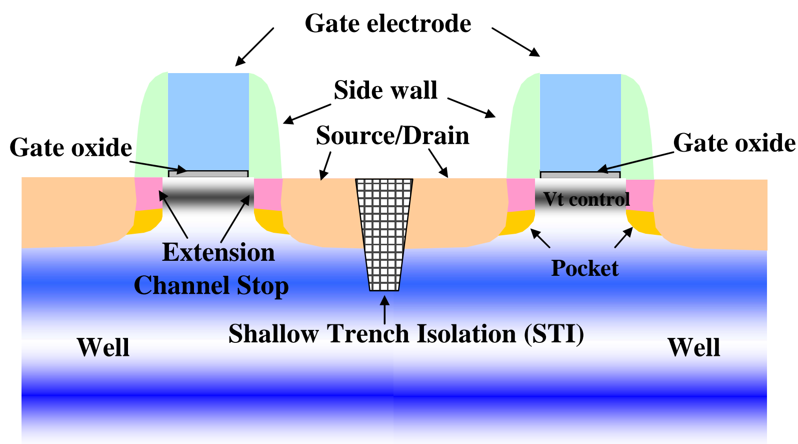

Fig.1-2. Cross-sectional View of a Typical Planar Bulk CMOS Transistor.

1.2.2. The Role of Ion Implantation in Fabrication Process of CMOS Devices

A cross-sectional view of a typical planar bulk CMOS n-channel transistor is shown in Figure 2. As the transistor gate length has been made shorter in recent years, an SDE (source drain extension) structure has begun to be employed [2] to suppress the short channel effect in the transistor due to the strong electric field which is generated in the source-drain gap and could lower the threshold voltage V_{th}. To be shallower with higher concentration is yet needed for this part. The required junction depth is about 10nm, and this is called the "shallow junction technology". The shallow junction

formation technology together with annealing technology is one of the most difficult technologies in semiconductor manufacturing. In implantation into the channel region to establish a suitable threshold voltage while suppressing the short channel effect, random variation of the ion doping distribution has become one of the most problematic issues [56].

(a) The Trend in Ion Implantation Technology for Shallow Junction Formation

For formation of a shallow junction at a depth smaller than 10 nm with a sheet resistance lower than 500 Ω/sq [2], it is essential that impurity doping is done at low energy, and that the heat treating to achieve high activation rate hardly causes diffusion of implanted atoms. In particular, lower energy implantation and channeling suppression has been pursued vigorously for the p-channel transistors, so that ^{11}B, with small mass number and high diffusion coefficient, can be used for the p-type impurity in the extension region. The implanter performance required for a junction formation at a depth of the order of 10 nm under the condition of complete suppression of channeling is an extremely low energy of a few 100 eV and a high dose of 5×10^{14} cm^{-2} with high throughput of about 200 sl/h for ^{11}B ion implantation. Successful implantation of 500 eV ^{11}B ions has been done by a method of deceleration from about 1 keV, which enabled relatively high current. However, since perfect exclusion of the energy contamination by this method is not possible due to unexpected neutralization of the beam ions, the perfect control of the depth profile is difficult. In addition, since ^{11}B has a relatively light mass, the beam is susceptible to space charge expansion which makes the beam transport difficult and a high current hardly obtained.

Pre-amorphizing implantation with Ge is a pioneering technology aiming at suppression of channeling and improvement of activation rate. During the preliminary

implantation before the ^{11}B implantation, an amorphous layer is formed on the Si substrate, which prevents the channeling of ^{11}B, and is an effective technique to improve the activation rate during annealing [16]. However, it could not totally satisfy the requirements of increasingly low energy and high concentration.

Cluster ion implantation is one of the most promising approaches that could solve the above problems of low energy implantation of ^{11}B**.** Large molecules or clusters consisting of a few to thousands of atoms are singly ionized and accelerated at medium voltage to minimize the space-charge expansion. Each atom has very low energy, however, and the atoms are lumped together until they impinge onto the surface of the substrate. Currently, investigations are under way [18] for the practical use of boron hydrides such as decaborane ($B_{10}H_{14}$) [17] and octadecaborane ($B_{18}H_{22}$) etc. Another merit of using cluster ions is the self-amorphizing effect of the massive cluster ion. This effect boosts the high activation rate obtained in the annealing process.

Since a He plasma has a similar effect of pre-amorphization [41], plasma doping method has been expected to be one of the promising technologies with potential feasibility. However, it is thought that the imperfect reproducibility could be an insurmountable obstacle to be overcome for commercial use.

Thus, it is generally agreed that control of the amorphized layer formed by ion implantation damage in the Si substrate is one of the most important factors for shallow junction formation.

(b) The Trend in Annealing Technology

Annealing technology has accomplished drastic changes in order to make the shallow junction. With development starting in the 1980s, when the transistor gate dimension was reduced from 0.5 μm to 0.35 μm, the “rapid thermal annealing” (RTA)

method appeared in the mass production lines in the second half of the 1990s [19,20]. This was a revolutionary change which replaced the conventional "vertical pipe furnace" annealing method requiring more than several hours, where the temperature elevation rate was a few ˚C/min, with the method which implemented fast temperature elevation of several tens of ˚C/sec and a short retention time at the top temperature of less than 10 seconds.

As device miniaturization progressed, with the start of the "0.09 μm generation", the "spike anneal" method [21] was introduced, which brought forth temperature elevation rates of several hundreds of ˚C/sec and a top temperature retention time of "0" seconds. To realize additional miniaturization, the so-called "msec-anneal" methods have been introduced, such as the "laser annealing" [22] and the "flash lamp annealing" [23]. In these methods, the density profile formed by ion implantation is retained after annealing as it is. Consequently, any variation in ion implantation is reflected directly to variation in the device characteristics.

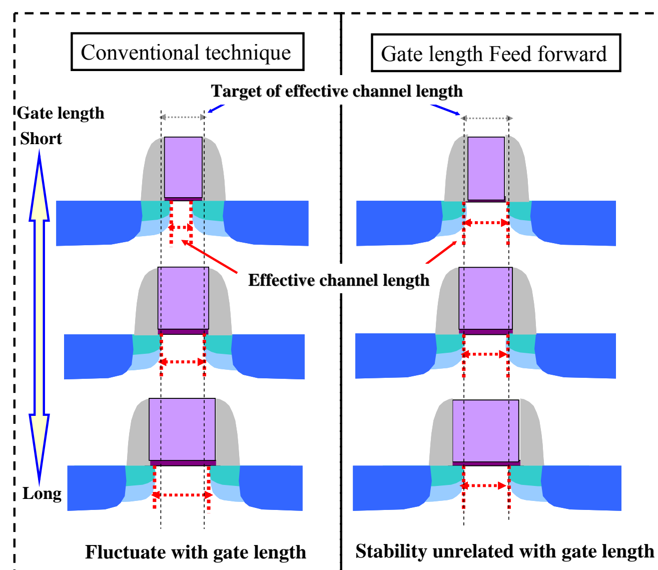

Fig. 1-3. Schematic explanation of Feed-forward Technology

(c) Technologies to Reduce Variability of Transistor Characteristics in Ion Implantation and RTA

Ion implantation and RTA technologies have especially high degrees of controllability compared with other semiconductor manufacturing technologies. Up to "the 0.1-μm gate" generation devices, there was sufficient margin for the implantation parameters. The "feed-forward" technology was developed to correct for any variations in the gate length brought about in the lithography and etching processes, and then to equalize the effective channel length. A schematic explanation is given in Fig. 3. The variation in the transistor characteristics caused by the variation in the gate length is compensated either by the implantation dose of the impurity and the annealing time.

Two methods have been developed and used as the typical feed-forward method. One is the method applying hybrid scan of the implanter beam in the medium-current system. The beam scan speed is controlled to correct the dose to match the required characteristics [24]. The other is the feed-forward to the annealing time in the RTA process [25]. Generally, the threshold voltage is approximately quadratically dependent on the gate length within a restricted range of the size, and is approximately linearly dependent on the annealing time. In this method the annealing time is controlled to compensate the threshold voltage variation due to the dependence on the gate length. Both of these methods are valid on the assumption that the implanter beam current is completely stable.

1.2.3. The Role of Ion Implantation in Fabrication Process of CCD Image Sensors

Figure 4 shows a schematic of the cross-sectional view of a typical CCD image sensor. To compensate for the unavoidable reduction in the light-receiving area in exchange for increase in pixel density, photodiodes must have greater depth. The

requirements for ion implantation technology for the current CCDs is “deeper, and at a low concentration of the order of 1×10^{11} cm^{-2}”. Moreover, since the characteristics of the photodiodes in the Si substrate are determined solely by the ion implantation, an accuracy of better than 1 % is needed in the ion implantation process. The difficulty of realizing 1 % accuracy is illustrated by the following example.

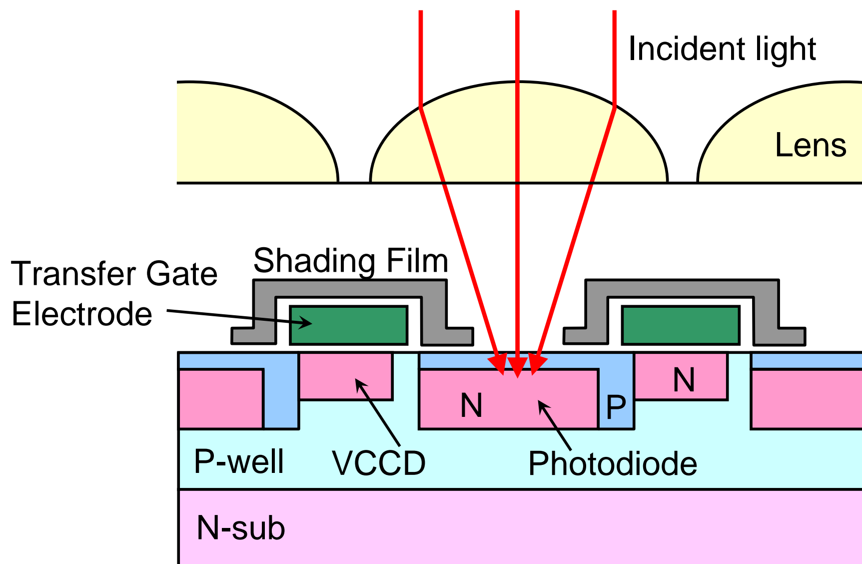

Fig. 1-4. Cross-sectional View of a CCD Device.

The size of cutting-edge CCD photodiodes is approximately 1.5 μm × 1.5 μm. If ion implantation of $1{\times}10^{11}$ cm^{-2} is carried out for this region, the number of impurity atoms implanted in 1one photodiode pixel is, 2.25×10^{3} atoms, and 1 % corresponds to 22.5 (atoms). This is means that control at the atomic level is required.

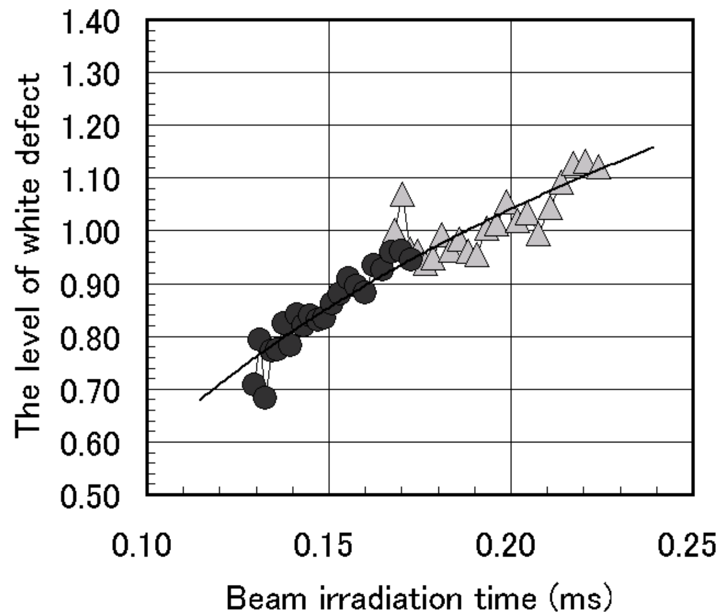

Fig. 1-5. Relation Between Ion Beam Irradiation Time and the Level of White Defect.

Another serious issue with CCDs is the so-called white defect. The white defect is the imperfect pixel unable to give photoelectric signal regardless of the input light intensity, and is said to be caused mainly by heavy metal contamination or crystal defects introduced into the Si substrate during the ion implantation. Dependence of the white defect level and the beam irradiation time is shown in Fig. 5 [26]. Only a few millisecond differences in exposure time leads to difference in the white defect level. This means that the damage of the atomic-level caused by the ion beam irradiation has the major impact on the device performance.

1.2.4. Measurement Technology

Evaluation techniques that have primarily been used to date in-line for general ion implantation systems and/or annealing systems include the four-points probe sheet-resistance measurement method and the thermal wave method. However, these methods measure the bulk properties, but cannot directly observe the implanted

impurity atoms, the crystal defect, nor the local damage in the semiconductor material. On the other hand, aiming at evaluation of phenomena of atomic level to meet the demand for the recent rapid miniaturization, there has been a rapid progress with microscopic measurement techniques, such as Secondary Ion-microprobe Mass Spectrometry (SIMS), a general evaluation method for implanted impurities, the three-dimensional atom probe (3DAP) [27], and scanning spreading resistance microscopy (SSRM) [28]. All of these are, however, destructive analysis techniques and cannot be used in-line in practice at a mass production facility.

1.3. Significance and Purpose of the present Study

It can be said that Si semiconductor device miniaturization has been supported by the high controllability in ion implantation technologies. Nevertheless, to the next-generation semiconductors, where the gate dimension approaches about 20 nm, the conventional methods of mechanical and electrical control of the ion beam can hardly be applied. It is necessary to clarify the mechanism by which the damage occurs. To this end an effective method is to visualize the interaction of the ion beam with the semiconductor material irradiated.

The main purpose of the present study is the development of methods to evaluate the damage caused by the ion beam irradiation in semiconductor material. In particular, issues such as variations of characteristics caused by ion implantation are often raised at mass production facilities rather than in research laboratories. The topics of the present research are focused on possible evaluation methods which are both in-line and non-destructive.

The first assignment, which is absolutely imperative, is to establish a method to

evaluate the film thickness of the amorphized layer formed in the process of shallow junction formation. At the present time, the amorphized layer thickness is determined by cross-sectional transmission electron microscopy (X-TEM). The amorphized layer required for the extension is formed with a dose in the 1×10^{14} cm^{-2} range, and the amorphous–crystalline boundary is rather indistinct. In the TEM determination of the film thickness, some ambiguity arises because of individual differences in the way the interface is identified depending on the engineer's subjectivity. In the present study, using spectroscopic ellipsometry (SE) for determination of the amorphized layer thickness is examined. As the SE method has been widely adopted as a measuring instrument in semiconductor manufacturing facilities, in-line evaluation would be possible. Accordingly, how the ion implanter conditions and the amorphized layer film thickness are related will also be clarified in detail.

The second assignment is to establish a method to evaluate the cross-contamination occurring during ion implantation. There are three types of cross-contaminations. One is energy contamination, which is referred to as the phenomenon that some of the dopant impurity ions are implanted at unintended energies because of charge-changing reactions during acceleration. Exclusion of these ions is accomplished in recent ion implanters by having an energy filter set up just before the wafer using a magnetic and/or electric field. The second is metal contamination. Transition metals immixed during ion implantation have a significant impact on emergence of white defects in CCD's. For this reason, ion implanters have been employing aluminum alloy for structural materials such as the beam line and the end station. However, it has become understood that even the amount of the transition metals contained in the aluminum alloy can cause the CCD white defect. In recent implanters, measures such as Si coating

of the aluminum alloy used on the beam line and around the wafer have been taken. As a result, immixing metal contamination during implantation has been suppressed almost down to below the detection limit. The third is cross-contamination which is the phenomenon that unintended immix during implantation as impurity dopants. Cross-contamination occurs mainly by sputtering of atoms implanted in the beam line components, especially in the surrounding area of the wafer, that were used as dopant ions in the previous implantation runs. It is an unavoidable phenomenon in the current state of the ion implantation technology with diversifying processes. the present study a technique to evaluate cross-contamination using the Particle Induced X-ray Emission (PIXE) analysis method is developed, and the cleaning effect of an Ar beam is discussed.

The third assignment is to set up an evaluation method for the charging phenomenon which is caused by deterioration of the photo-resist mask due to irradiation damage during the ion implantation. The way in which the photo-resist deteriorates is verified by the TOF-SIMS method as well as the SE to ascertain the deterioration mechanism. In addition, the effect of surface potential changes, which are closely related to the deterioration, on the control of the implantation dose which should otherwise be perfect, is examined.

1.4. Structure of the dissertation

The present dissertation is composed of the following five chapters.

Chapter 1 is an introduction, which has discussed the current status of the ion implantation technology for Si-based semiconductors especially the implantation accuracy with examples of CMOS and CCD devices. Based on these considerations, the issues for establishment of the method to evaluate the damage in semiconductor

material caused by the ion beam have been classified, and the objective of the present research has been stated.

In chapter 2, a proposal of a simple and in-line method using the SE is put forward to measure the amorphized layer thickness. The determination of the amorphous–crystalline boundary is extremely important in the evaluation of the pre-amorphized layer. The amorphized layer thickness defined on the TEM image is compared with the thickness measured with high resolution Rutherford backscattering spectroscopy, HR-RBS, and that with the SE. Based on this result, the relations between the film thicknesses and the width of the highly- damaged region of the amorphous–crystalline boundary transition region is discussed. This region is very sensitive to its thermal history, and is expected to be useful for evaluation of the ion implanter conditions. Therefore, the amorphized layers formed under various conditions are evaluated using the SE, and the relationship between the ion beam conditions and the Si substrate irradiation damage will be examined.

In chapter 3, the grazing angle-incidence PIXE method is examined as a technique to evaluate cross-contamination. The target value of the detection limit for the CMOS device extension region having atomic density of ($5\times10^{14}/cm^2$, was set at 1%, i.e., $5\times10^{12}/cm^2$. Utilizing the grazing angle-incidence PIXE method to increase the irradiated area and use of a dummy surface to reduce the bremsstrahlung background X-ray signals are examined. Moreover, the technique is applied to detection of cross-contamination with a density of the same order of magnitude.

In chapter 4, the charging phenomenon, which occurs during the ion implantation onto the photo-resist surface, is evaluated by making use of a surface potential measurement tool. It is inferred that the molecular bonds of the photo-resist begin to be

cleaved preferentially at bonds with smallest binding energy, and cross-linking begins to form a low-resistance carbonized layer. A Monte Carlo simulation is performed to calculate the implanted atoms and the recoil atoms to discuss the critical implantation dose for carbonization. Moreover, the relationship between the formation of the low resistance layer on the photo-resist surface and the local breakdown of the accumulated charges is discussed. Finally, the possibility is discussed that the charging phenomenon discussed above is the cause of the so-called explosion phenomenon as well as implantation dose fluctuations occurring in mass production facilities.

Chapter 5 is the conclusion to the above studies, summing up the results from chapter 2 through chapter 4 in block, and future perspectives are mentioned.

Chapter 2. Evaluation of Pre-Amorphized Layer Thickness and Interface Quality of High-Dose Shallow Implanted Silicon by Spectroscopic Ellipsometry

2.1. Introduction

In shallow junction formation, the thickness and quality control of the pre-amorphized layer is an important element. Its accurate measurement and precise control are essential for quality control in device manufacturing.

Fluctuations in the thickness of amorphized layers created by accumulation of damage from ion implantation can cause variations in dopant diffusion [29, 30] and activation [31] and leakage current [32]. Control of junction leakage current is of particular importance for many IC applications. Residual implant defects near or in the junction depletion layer [32] can cause severe junction leakage problems. The major sources of residual defects [33] after annealing are various forms of "end of range (EOR)" defects formed just below the amorphous/crystalline interface. The thickness of the amorphized layer formed by an ion implantation process is mainly determined by implant conditions (ion mass, implantation energy, ion dose, implantation angle etc.) and directly affects the depth and density of the EOR defects, dopant diffusion, dopant activation and junction leakage [31]. Practical operational factors of ion implantation, such as ion beam current density, scan rate and wafer temperature during implantation [34-36], as well as the type of implanter used, can also introduce noticeable variations in the thickness of the amorphized layer and quality of interface including EOR defects. To effectively maintain the quality of the production process, a reliable in-line Pre-amprhization layer monitoring technique must be developed for statistical process control (SPC) and day-to-day implanter tuning/matching.

Rutherford backscattering spectroscopy (RBS) and cross-sectional transmission electron microscopy (X-TEM) have been used to measure the amorphized layer thickness. However, these are destructive measurement techniques and require wafer breakage and/or sophisticated sample preparation. Due to these reasons, RBS and X-TEM are not suitable as in-line process monitoring techniques. Spectroscopic ellipsometry (SE) is a non-destructive amorphous layer thickness measurement technique with good spatial resolution (spot size 28 μm). It has been used for the amorphized layer thickness measurement after implantation (>20 keV) [37] and solid phase regrowth at low annealing temperatures [38-40].

In this work, a comparative study of the thickness measurement of amorphized layers after low energy (<20 keV), low dose (3×10^{14} ions/cm^2) As ion implantation by SE, RBS and X-TEM techniques has been performed. An application of the thickness measurement using the SE technique has also been demonstrated for the amorphized layers formed by He^+ implantation by plasma immersion methods [41, 42].

2.2. Experimental Details

2.2.1. Sample Preparation

Two hundred millimeter (200 mm) p-type Si (100) wafers with a resistivity of 10-15 Ω-cm were used in this study. The wafers were implanted with As or Ge ions using a batch-type high current ion implantation machine (disk rotation speed: 1200 rpm) at energies from 4 to 30 keV with doses from 2×10^{14} to 5×10^{14} ions/cm^2 to form amorphized layers on the surface. Typical implant energy and dose for shallow junction formation were selected. All wafers were implanted with a fixed beam current of 1 mA. The disk and wafer cooling fluid temperature was controlled at a set point of 23 ^{o}C to

keep wafer temperature at 100 ^{o}C or less during ion implantation.

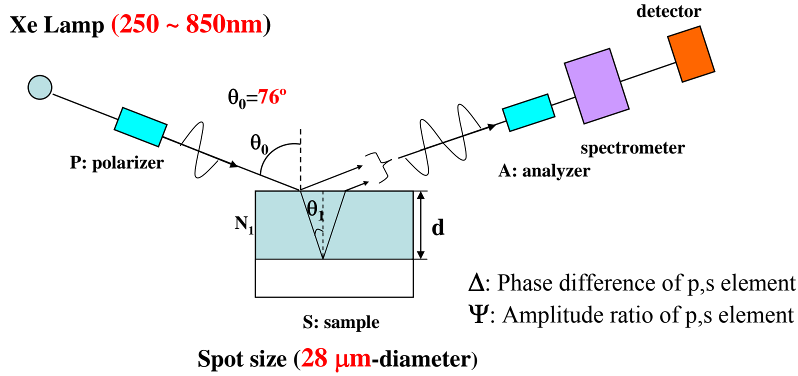

Fig. 2-1. Schematic diagram of spectroscopic ellipsometry.

2.2.2. Thickness Measurement Technique

A schematic diagram of SE is illustrated in Fig. 2-1. An SE system was used in this study. The system uses a Xe-lamp as a light source in the wavelength range of 250 to 850 nm (KLA-Tencor, F5X, Summit software Version 2.6). The system spec of the beam spot size for the F5X, KLA-Tencor, is 28 × 21 μm at the surface of the measurement sample when the incident angle is 76°.

SE measures the amplitude ratio (Ψ) and change in phase difference (Δ) of the p- and s-polarized light after reflection from a sample surface. And these elements are known to be a function of N (the complex refractive index) and d (the film thickness) [43, 44]. The complex refractive index N ($N = n - ik$: n = refractive index, k = extinction coefficient) of a samples with perfect flatness and infinite thickness can be expressed as follows;

$$n^2 - k^2 = \sin\theta_0 \left(1 + \frac{\tan^2\theta_0 \left(\cos^2 2\psi - \sin^2 2\psi \sin^2\Delta\right)}{\left(1 + \sin 2\psi \cos\Delta^2\right)} \right)$$

$$2nk = \frac{\sin^2\theta_0 \tan^2\theta_0 \sin 4\psi \sin\Delta}{\left(1 + \sin 2\psi \cos\Delta^2\right)}$$

where θ_0 is the Angle of incidence.

This formula is applied here to the amorphized layer as an approximated expression.

RBS measurements were made by a high resolution RBS (HR-RBS at a Kobe Steel Group Company facility) [45]. The helium probe ions were irradiated with an incident energy of 450 keV at an angle of 45˚ to the normal of the sample surface, and the scattered helium ions were detected by a polarizing magnetic field-type energy spectrometer with a scattering angle of 77˚. For calculation, a Si density value of 2.2 g/cm^3 and SiO_2 density value of 2.33 g/cm^3 were used.

X-TEM lattice images were taken using a TOPCON microscope with electron energy of 200 keV. The magnification of images was determined on the basis of the Si lattice spacing.

2.3. Result and Discussion

2.3.1. Amorphized Layer Thickness

All measurement techniques (SE, HR-RBS and X-TEM) used in this study showed consistent trends of amorphized layer thickness increase with the increase of ion implantation energy at a given dose condition.

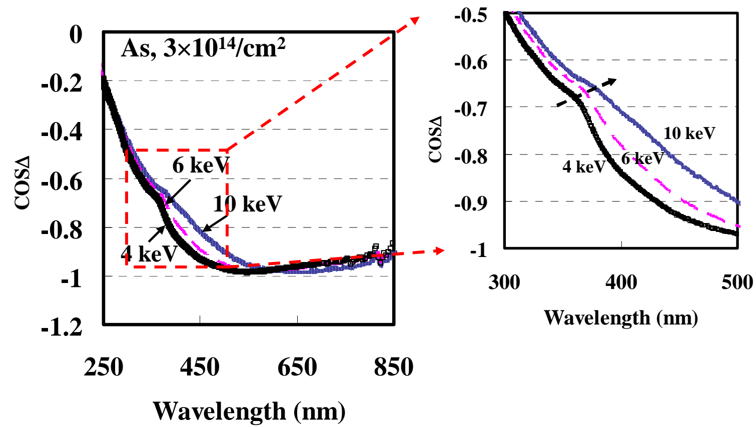

(a)

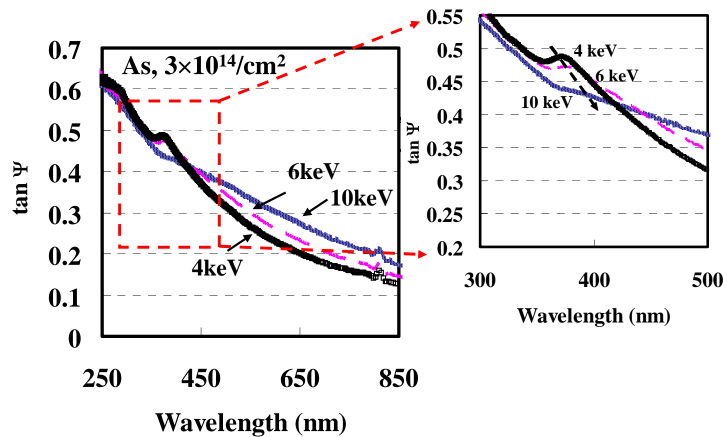

(b)

Fig. 2-2a, 2b. The spectrum of cosΔ (a) and tanΨ (b) measured by SE for As ion implanted silicon.

Figure 2-2 (a) and 2 (b) show the spectra of cos Δ and tan ψ components measured by SE from As implanted Si with implantation energies ranging from 4 to 10 keV and a fixed dose of 3×10^{14} ions/cm^2. As seen in the figures, noticeable change of spectra was observed between wafers with different implantation energy. The shoulder of the spectra shifts in the longer wavelength direction and the slope of spectra becomes less as As ion implantation energy increases. The SE spectra are sensitive to the ion implantation energy at a given dose. Since the thickness of the amorphized layer

depends on the implantation energy and dose, the SE spectra can be used as a non-destructive, in-line monitoring technique for amorphized layer thickness.

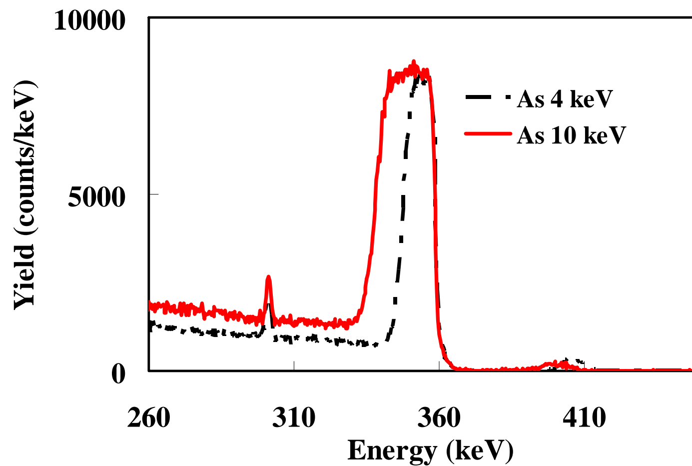

Fig. 2-3. HR-RBS spectrum of the amorphous layer measured using a 450 keV H^+ beam.

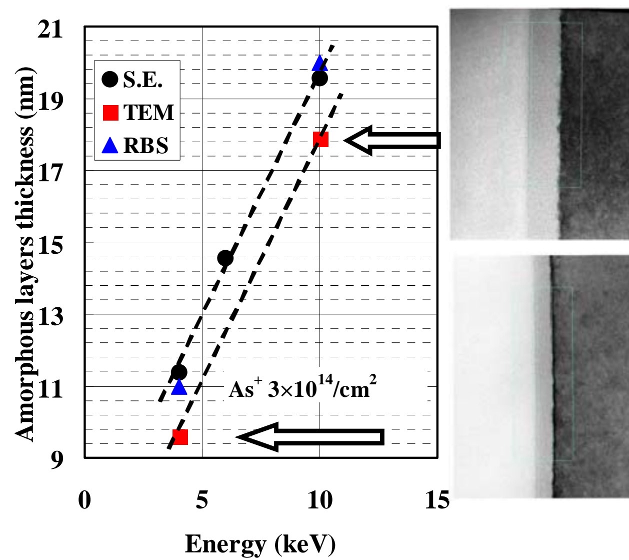

Fig. 2-4. The amorphous film thickness dependence on implanting energy for three measurement methods (●: SE, ▲: HR-RBS, and ■: X-TEM).

High resolution Rutherford backscattering (HR-RBS) measurement in channeling mode operations is useful in analyzing the crystalline damage and dopant profiles in Si

for all dopants except for boron and phosphorous. HR-RBS spectra from As implanted Si with implantation energies of 4 keV and 10 keV, at a dose of 3×10^{14} ions/cm^2, are shown in Fig. 2-3. The vertical axis of yield per unit energy (or channel) depends on the amount of impurity atoms, including Si atoms, out of crystalline Si lattice sites. The horizontal axis of energy (per channel) depends on the mass and depth of impurities. Thus the main channeling peak can be interpreted as the thickness of the amorphized layer by ion implantation as indicated in Fig. 2-3. The width of the Si signal became wider as As energy increased from 4 keV to 10 keV at a fixed As dose of 3×10^{14} ions/cm^2. This is a firm indication of dependence of the amorphized layer thickness on ion implantation energy.

The amorphized layer thickness estimated by three measurement techniques (SE, HR-RBS and X-TEM) is summarized as a function of As ion implantation energy at a fixed As dose of 3×10^{14} ions/cm^2 in Fig. 2-4. For SE measurement, several dielectric function models have been proposed so far for the homogeneous, amorphous layer formed by Chemical vapor deposition (CVD) etc. [46] However, there is a possibility that the optical constants of the amorphized layer formed by the ion implantation depends on the implanted impurity profile, and is inhomogeneous in the direction of depth. Moreover, there is a necessity for making them applicable to wide range of Ion implantation condition. Therefore, for the amorphized layer thickness calculated from the SE spectra, the harmonic oscillator model [47-49], with a high adaptability to wide range of the optical constants by having plural oscillators, is used assuming the top surface to be a single amorphous layer. And it calculated using four oscillators so that Chi-squared goodness of fit (GOF) might become 0.75 or more.

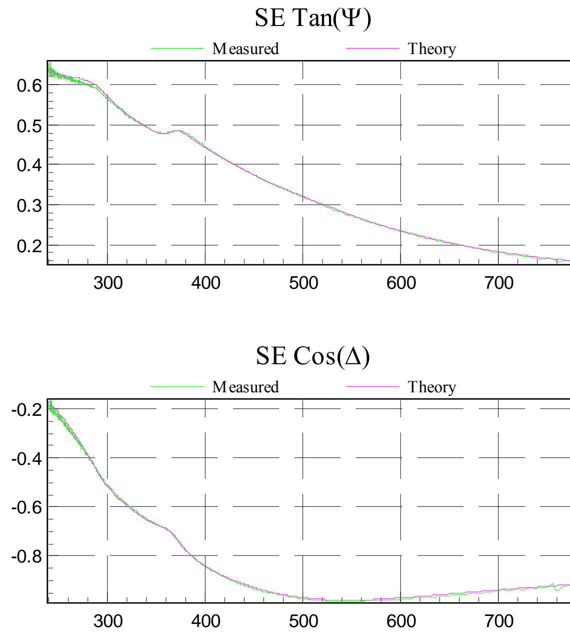

Fig. 2-5. The example of fit curve, at the As implantation energy of 4 keV and a dose of $3\times10^{14}/cm^2$, was calculated using our harmonic oscillator model.

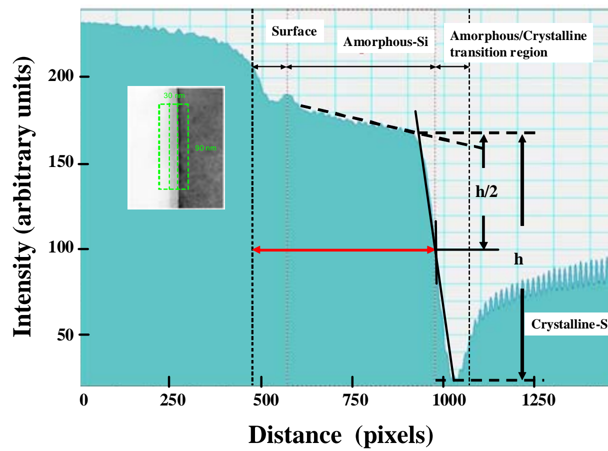

Fig. 2-6. Amorphized film thickness estimation from an X-TEM image. (The film thickness was estimated from numerically converted image contrast of an X-TEM image after image processing.)

Fig. 2-5 shows the example of fit curve, at the As implantation energy of 4 keV and a dose of $3\times10^{14}/cm^2$. It was calculated using our harmonic oscillator model. In this case, Chi-squared goodness of fit (GOF) was 0.84. The GOF decreases with increasing

energy and with decreasing dose. The value of 0.75 is the lowest one in our experiments. And the native oxide is not included in our model, because the usual SiO_2 model becomes inapplicable as the As ion implantation proceeds to produce knock-on and sputtering effect, etc. Therefore, the oxygen incorporation was abandoned in order to give priority to simplicity in use in the factory, at a cost of accuracy.

Table 2-1 shows the fundamental parameter of each oscillator used for this measurement.

TABLE 2-I

The fundamental parameter of each oscillator used for this measurement

	Noc (nm^{-3})	En(eV)	Eg(eV)	Nu	Φ(rad)
Osillator1	45.077	3.6222	2.6509	0.2773	0.3205
Osillator2	120.70	3.4900	2.1197	0.0496	-2.3460
Osillator3	75.416	3.9673	1.8739	-0.0142	0.0085
Osillator4	374.31	5.6653	14.058	-0.0292	1.0096

Noc=density, En=resonance energy, Eg=absorption energy,

Nu=compensation value of polarization quantity, Φ=phase difference,

These fundamental parameters were determined by analyzing a thick (70 nm or more) layer of Si amorphized by high energy and high dose ion implantation. [37], on the basis of Ref. [50].

The details of amorphized layer thickness estimation from X-TEM and HR-RBS are illustrated in Fig. 2-6 and Fig. 2-7, respectively. The amorphized layer thickness was measured from the surface marker to one half of the maximum contrast of the amorphous/crystalline transition tail using the image contrast after X-TEM image processing. From the HR-RBS spectra, the amorphized layer thickness was defined as

the width from the middle points of both edges of a Si signal.

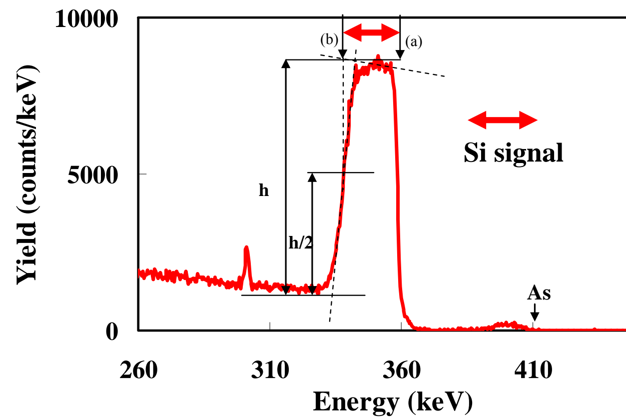

Fig. 2-7. Amorphized film thickness estimation from a HR-RBS spectrum. (The film thickness was defined as the width from the mid-point of the high energy side (a) to the mid-point of the low energy side (b) of a Si signal of HR-RBS spectrum.)

The thickness values estimated by all three measurement techniques came out to be similar. However, the values from SE and HR-RBS were ~2 nm greater than those from the X-TEM image processing. The difference can be understood as a contribution of uncertainty due to the amorphous-crystalline transition region such as interface roughness and contrast variations caused by sample preparation. It should be noted that the SE measurements are done at 49 points over the wafer surface and the average thickness value was used. On the other hand, the HR-RBS and TEM measurement was done at one location (the wafer center). These may have contributed to variations of estimated amorphized layer thickness. There is a possibility that the amorphized layer thickness values estimated by SE and HR-RBS include not only fully the amorphized layer, but also part of the amorphous-crystalline transition layer with heavy crystalline damage.

2.3.2. Discussions

The slope of X-TEM image contrast change near the amorphous/crystalline transition region depends on the roughness of the amorphous/crystalline interface (Fig. 2-8 (a) and (b)). For amorphized layer thickness estimates, the roughness of the amorphous/crystalline interface must be considered.

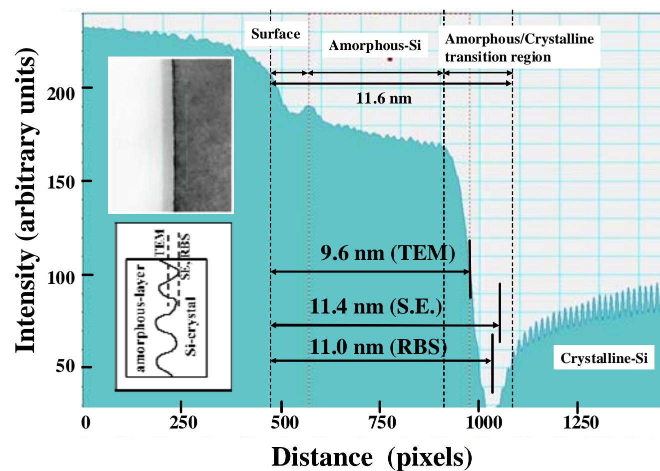

(a)

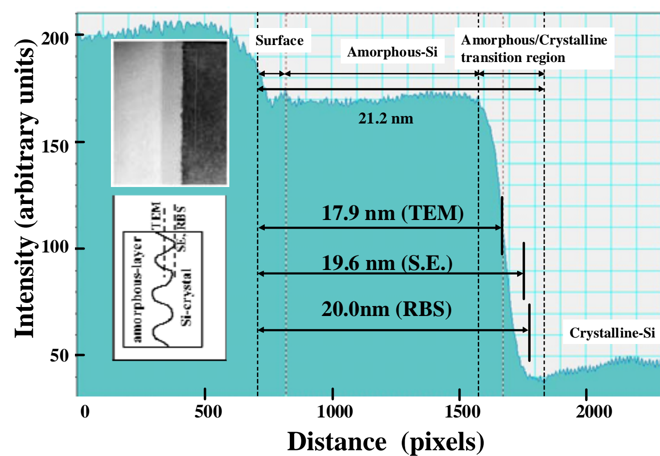

(b)

Fig. 2-8a, 8b. Comparison of amorphized layer thickness values estimated by SE and HR-RBS measurements on a numerically converted X-TEM image contrast. ((a) As-ion implantation at energies of 4 keV, at a dose of $3x10^{14}$ ions/cm^2. (b) As-ion implantation at energies of 10 keV, at a dose of $3x10^{14}$ ions/cm^2.)

The amorphization of the Si substrate is considered to be caused by collision cascades of recoil Si atoms under incidence of the implantation ions. To theoretically estimate the location of the amorphous/crystalline interface, the atomic concentration of recoil Si, at As implantation energies of 4 keV and 10 keV, was calculated using SRIM2008 [51] and plotted in Fig. 2-9 as a function of depth. The amorphized layer thickness values estimated by SE, HR-RBS and X-TEM were superimposed on the recoil Si depth profiles for comparison. For the As ion implantation (10 keV and 3×10^{14} ions/cm^2), the estimated by X-TEM is located at a recoil Si density of ~2.0×10^{22} atoms/cm^3. The depths estimated by various techniques shown in Fig. 2-8 (a) and (b) are located between a recoil Si concentration of 2.6×10^{23} atoms/cm^3 and 8.1×10^{22} atoms/cm^3. As implantation energy increases, the range of depth values estimated by various techniques maximum concentration of recoil Si exceeds the atomic density of crystalline Si (5.2×10^{22} atoms/cm^3). For the sake of qualitative discussion of the amorphization mechanism and location of the amorphous/crystalline interface, the inconsistency was ignored.

The depth of the amorphous/crystalline interface estimated by SE and HR-RBS is located at a recoil Si density of ~1.0×10^{22} atoms/cm^3. The depth widens. However, the recoil Si density simulation results in reasonably good agreement with experimental results. It seems that the thickness values estimated by the SE and HR-RBS are more sensitive to damage in the crystalline Si compared to X-TEM.

In the case of SE measurement, the average thickness of the amorphized layer in a measurement spot size of 28×21 μm in diameter is estimated and the average of 49 points across the wafer is given as a thickness value. Thus, the thickness value estimated by SE measurement can be very useful for characterizing the impact of ion implantation

in terms of pre-amorphized layer and amorphous/crystalline transition layer thicknesses.

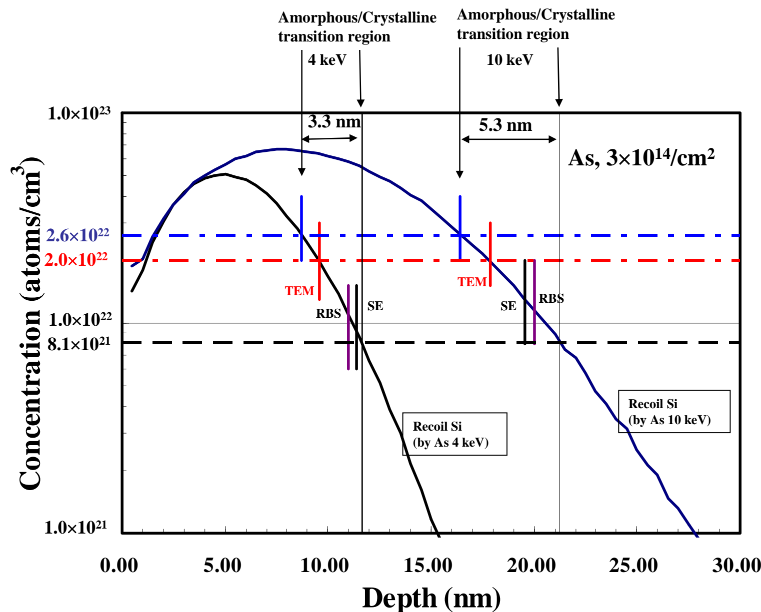

Fig. 2-9. Atomic concentration of recoil in Si for a fixed As dose of 3x10^{14} ions/cm^2 with implantation energies of 4 keV and 10 keV calculated using SRIM2008. (Thickness values of amorphized layer estimated by various techniques are superimposed.)

2.3.3. Roughness Evaluation of Amorphous/Crystalline Interface by SE

The possibility of evaluation of the roughness of the amorphous/crystalline interface was investigated using the sensitivity of SE on a heavily damaged region near the amorphous/crystalline transition layer. Si wafers implanted with As ions (10 keV, 3×10^{14} ions/cm^2) were annealed for 30 min at low temperatures (100 ^{o}C, 200 ^{o}C, 300 ^{o}C and 400 ^{o}C) in 1 atm N_2. To improve accuracy of the experiment, a single wafer rapid thermal furnace was used in this study. This system provides isothermal cavities for wafer processing and heats wafers primarily by natural convection. The details of the operating principles and features of the system has been reported by Yoo et al.[52, 53] The SE measurement results are shown in Fig. 2-10. The amorphized layer on single crystalline silicon has its crystalline structure restored by a solid phase regrowth

mechanism with relatively low temperature annealing, below 500°C. The activation energy of solid phase regrowth is reported to be 2~3 eV [54, 55]. However, the SE spectra starts to change even after annealing at lower temperatures, where the solid phase regrowth does not take place. The initial thickness of the amorphized layer was estimated to be 20.04 nm by the SE spectra. From the change of the amorphized layer thickness, estimated by the SE spectra after annealing for 30 min, the regrowth rate of crystalline Si was calculated. Wafer temperature ramp-up and ramp-down times were neglected for simplicity since the annealing time of 30 min is relatively long. Figure 2-11 shows an Arrhenius plot of the regrowth rate of crystalline Si near the amorphous/crystalline interface region. The activation energy associated with this regrowth is calculated to be 0.17eV. This value is more than one order of magnitude smaller than the values previously reported [54, 55]. Since the temperature range (475°C~575 °C and 500 °C~750 °C) of previous studies only covers the higher end of the temperature range (100 °C~500 °C) of this study, it is difficult to simply compare the values without going through further investigation. However, the very small activation energy of 0.17 eV implies that the low temperatures (as low as 100 °C) can influence the amorphous/crystalline interface region which results change in the SE spectra and the recrystallization of the amorphized layer from the interface.

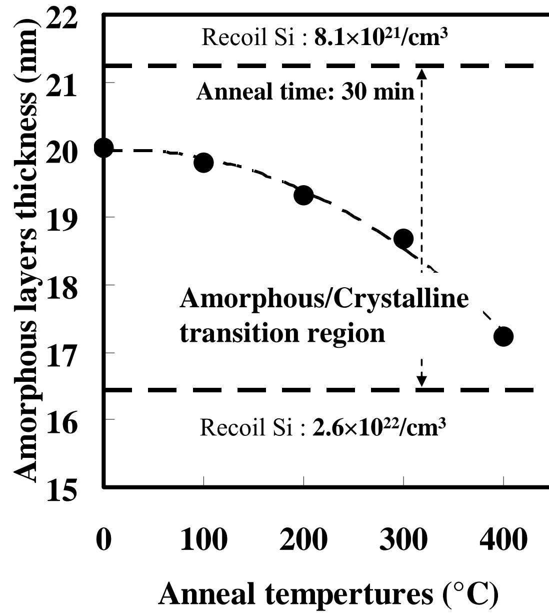

Fig. 2-10. Amorphized layer thickness measured by SE before and after low temperature annealing at 100 °C~400 °C.

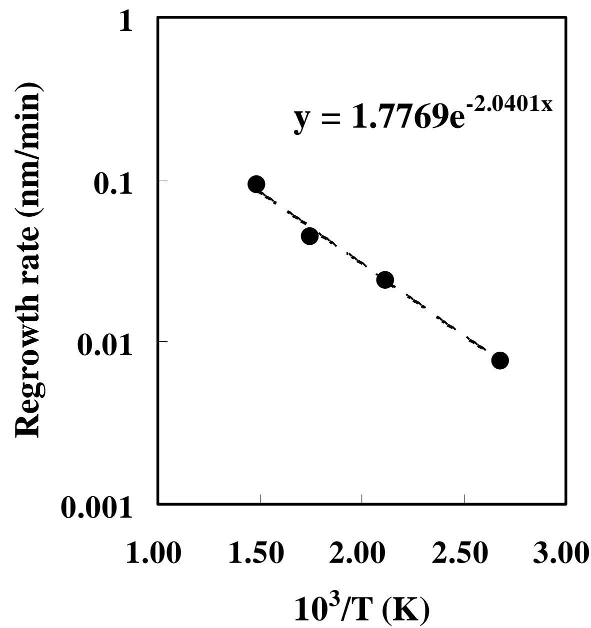

Fig. 2-11. Arrhenius plot of regrowth rate of the amorphized layer in the temperature range of 100 °C~500 °C. (Ion implantation conditions: As 10 keV, $3x10^{14}$ ions/cm^2)

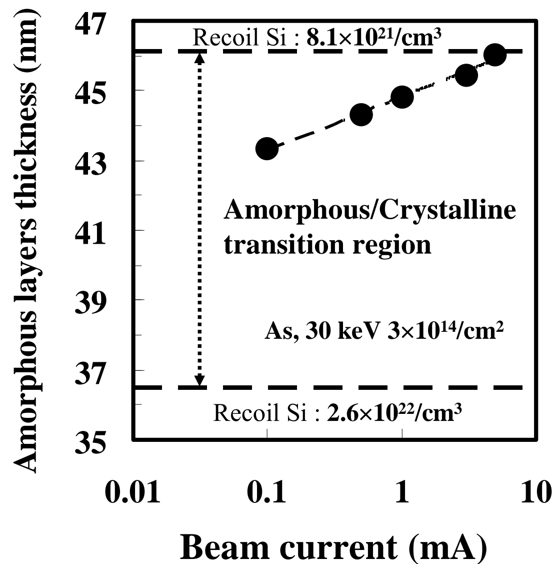

Fig. 2-12. Amorphized layer thickness variation measured by SE as a function of ion beam current at a fixed As-ion implantation energy of 30 keV and a fixed dose of $3x10^{14}$ ions/cm^2.

The SE spectra indicate slight reduction of the amorphous layer thickness, even after low temperature annealing. It is very sensitive to the thermal history of amorphized layers. The SE measurement treats the heavily damaged layer as a part of the amorphized layer. This sensitivity of detecting the heavily damaged layer can be very useful in characterizing the roughness of the amorphous/crystalline interface. It can also be used for monitoring the performance and conditions of individual implanters (such as for fluctuations of wafer temperature, implantation energy, beam current density and beam scanning etc.).

Beam current dependence of amorphized layer thickness after As-ion implantation at an implantation energy of 30 keV and dose of $3x10^{14}$ ions/cm^2 is plotted in Fig. 2-12 as a function of ion beam current during implantation. As the beam current increases, the amorphized layer thickness, measured by SE, increases slightly within the range of interface roughness. This indicates the increase of the thickness of the heavily damaged

layer by the increase of ion beam current at a given implantation energy and dose. The SE measurement can detect the fluctuation of beam current at a given implantation energy and dose with thickness variation of the amorphized layer.

2.4. Applications

The thickness of an amorphized layer changes not only with ion implantation process conditions (ion species, energy, dose) but the also with the ion implanter conditions (wafer temperature, implantation energy, beam current density, beam scan. etc.). Therefore, it is very important to have a non-destructive, in-line amorphized layer thickness measurement technique. The SE can be very suitable for this application.

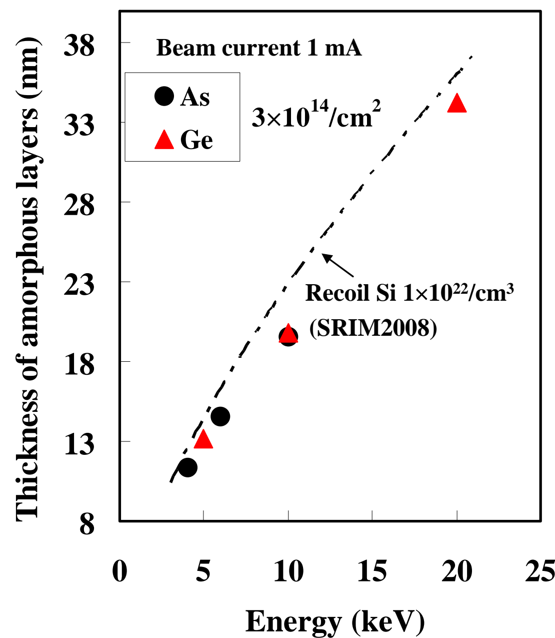

Fig. 2-13. Amorphized layer thickness of Ge-ion and As-ion implanted Si wafers measured by SE as a function of implantation energy at a dose of $3x10^{14}$ ions/cm^2.

2.4.1. Pre-amorphization by Ge and As Ion Implantation

The thickness of the amorphized layer formed by ^{72}Ge and ^{75}As ion implantation measured by SE, is plotted in Fig. 2-13 as a function of implantation energy. The implant dose was fixed at 3×10^{14} ions/cm^2 for all samples. Since the atomic mass of Ge and As are similar, both the implantation damage to the Si and the thickness of the amorphized layer showed similar trends. The thickness of the amorphized layer increases proportionally to the increase in implantation energy.

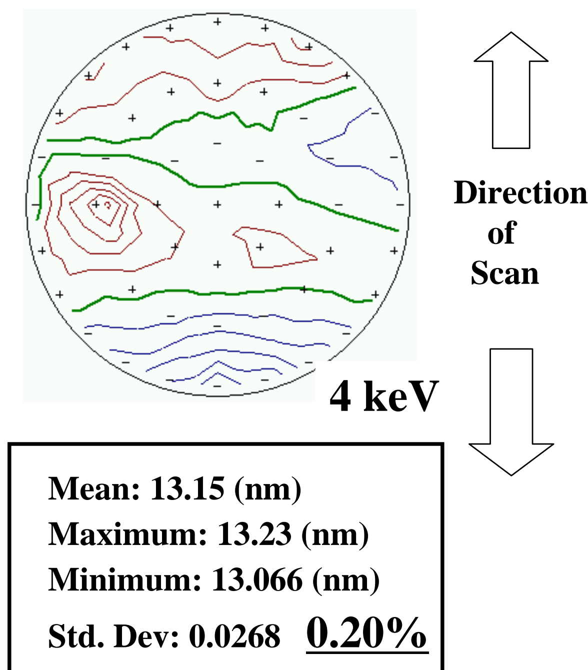

Fig. 2-14. Amorphized layer thickness uniformity map (49 point measured by SE) of a Si wafer after Ge implantation using a batch type ion implanter.

Fig.2-14 shows a 49 point cross-wafer uniformity map of the amorphized layer thickness measured by SE after Ge implantation using a batch type ion implantater. The Ge ions were implanted at an energy of 4 keV and a dose of 3×10^{14} ions/cm^2. The standard deviation of the amorphized layer thickness over the wafer was 0.2 nm or less. However, the signature of the beam scanning (disk translation direction), inherent to the

batch type implanter, can still be seen in the amorphized layer thickness map.

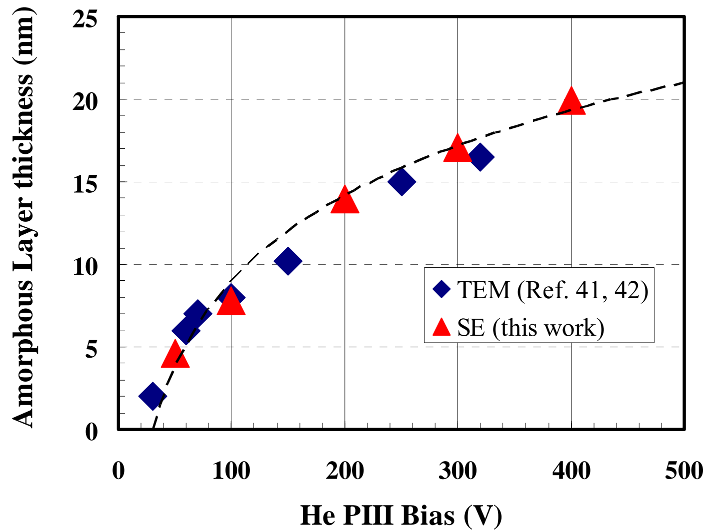

Fig. 2-15. Amorphized layer thickness of He+ PIII implanted wafers measured by TEM (Ref. 41, 42) and SE (this work) as a function of He PIII bias voltage.

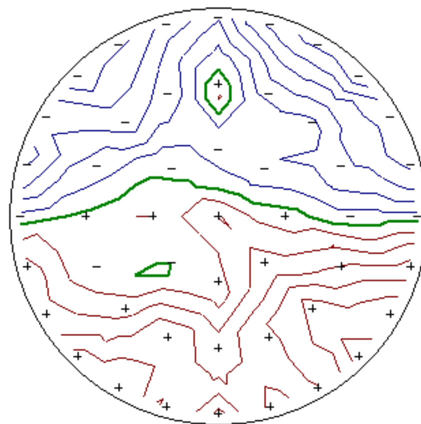

Mean: 7.79 (nm)
Maximum: 8.06 (nm)
Minimum: 7.51 (nm)
Std. Dev: 0.146 **<u>1.87%</u>**

Fig. 2-16. Amorphized layer thickness uniformity map (121 point measured by SE) of a Si wafer after He+ PIII implantation with a bias power of 100W.

2.4.2. *Amorphization by He RF Plasma Doping*

It is well known that high-dose, shallow implantation in plasma doping amorphizes the Si surface [41, 42]. The thickness and uniformity of the amorphized layer formed during He RF plasma doping for 30 s was measured by SE (Table 2-2). The amorphized layer thickness of Si wafers implanted by He^{+} Plasma Immersion Ion Implantation (PIII) and measured by X-TEM (Ref. 41, 42) and SE (this work) is summarized in Fig. 15 as a function of He PIII bias voltage. It shows that the amorphized layer thickness is mainly determined by the bias voltage (or power) while other plasma doping conditions (plasma density, He ion dose, pulse repetition rate and wafer temperature during implant. etc.) have negligible effect on the amorphized layer thickness.

TABLE 2-II

The amorphous layer thickness for helium plasma immersion implant

Bias Power (peak to peak voltage)	100W (100 V)	400 W (200V)
Thickness (nm)	7.79	19.9
Uniformity (%)	1.89	1.12

The amorphized layer thickness map of a typical wafer implanted in PIII with a bias of 100 W is shown in Fig. 2-16. A 49 point SE measurement shows the thickness uniformity of the amorphized layer is 2 % or less. There is a possibility that the uniformity of amorphized layers formed in He plasma doping can further be improved by utilizing the in-line monitoring capability of SE in process optimization.

2.5. Conclusion

The pre-amorphized layer thickness formed by ion implantation has been measured using SE, HR-RBS and X-TEM methods. The amorphized layer thickness measured with SE appears to be measuring from the wafer surface into the heavily damaged region, below the amorphized layer imaged by TEM. The thickness measured by SE gives almost the same value estimated by HR-RBS. The thickness measurement of the amorphized layer using SE provides an accurate measurement (within 2 nm) and high sensitivity of the heavily damaged layer near the amorphous/crystalline interface. It is a non-destructive and non-contact measurement technique which enables rapid, multi-point mapping of thickness over a wafer. It is also a very attractive and powerful measurement technique for in-line monitoring of amorphized layer thickness as well as implanter conditions.

Chapter 3. New Evaluation Method for Cross-contamination of Ion Implantation by Using Grazing Angle Incidence PIXE in Photo-resist

3.1. Introduction

The ion implantation technology is used in the semiconductor manufacture over a wide range of process conditions, i.e., energy from 100eV to a few MeV, and dose (defined here as the number of dopants implanted per unit area) from $1\times10^{11}/cm^2$ to $1\times10^{17}/cm^2$. Accurately understanding the quantity of impurities, both intentional and accidental, introduced in the Si substrate by the ion implantation, as the requirement of scaling and high performance of the semiconductor devices, becomes increasingly important. [56]

Since it is common practice to implant a variety of dopant and other ions in the same implant tool, cross-contamination, or the unintentional delivery of elements from a previous implant cycle, is a continual area of concern. The mechanisms by which cross-contaminant elements can arrive at a wafer during implant include insufficient mass resolution settings as well as sputtering and vapor deposition from electrodes, beam stops and other beam-line surfaces [57]. Cross-contaminating dopant species can result in anomalous shifts in junction depth at contamination levels as low as 0.01% [58]. Metallic impurities in Si, such as Fe, Ni, Cr, and Ta, at levels of the order of 1 ppb can lead to reductions in carrier mobility and lifetime as well as large increases in junction leakage currents. With typical high dose implants at $\approx10^{15}$ ions/cm^2, an efficient in-line method for detection and identification of dopant and metallic contaminants at the level of $\approx10^{12}$ atoms/cm^2 (0.1 %) is highly desirable.

In usual practice, the dose of an ion implant is measured indirectly, with sheet

resistance metrology by using 4-points probe measurements or by Junction Photo-Voltage (JPV) methods, or by monitoring the accumulated damage by using thermal wave or other optical reflection methods [59, 60]. However these methods are not suited for quantitative detection of small amounts of contaminant atoms. Sheet resistance methods require the formation of p-n junctions to detect effects of dopant cross-contaminants and are unable to monitor metallic and other non-dopant contaminants.

Another method for analysis of impurities in the substrate is secondary ion mass spectrometry (SIMS) [61]. This method can analyze the depth profile of the ion implantation impurities with high spatial resolution. However, SIMS has difficulties distinguishing the atomic number, chemical identity, of contaminant species. Also SIMS is a destructive inspection; sputtering removal of the sample is necessary to know the depth distribution and the dose integrated over some depth.

On the other hand, application of characteristic X rays emitted by particle (electrons, ions or X-ray photons) beam incidence for measurement of the ion implantation impurities has been successful in some practical cases.[62, 63, 64] This method is a nondestructive analysis. However, the minimum areal density of impurities in the Si substrate detectable by using these methods, i.e., the sensitivity, is about $1\times10^{14}/cm^2$. This limit is set by interference of background bremsstrahlung radiation emitted in the process of deceleration of the probe beam particles in the substrate.

Total Reflection X-ray Fluorescence (TXRF), is a nondestructive surface analysis technique, that has a high sensitivity in the vicinity of the surface shallower than about 10 nm. TXRF is not applicable, however, to the measurement of implanted impurities, because of the implanted density distribution can extending to several tens of

nanometers or more [65].

In the present work, Particle Induced X-ray Emission (PIXE) analysis has been used to analyze the impurities on photo-resist layers formed over the Si wafer to measure the number of implanted and cross-contaminant arsenic (As) atoms, and to investigate the use of accelerator analysis as an in-line impurity monitor. PIXE analysis is an analysis technique widely used in the field of environmental science, biology, medical science, and archeology, etc. [66]. It is a nondestructive method that measures characteristic X-rays excited by a several-MeV proton probe beam incident on the sample target. When impurities in a Si substrate are analyzed by using this method, the bremsstrahlung radiation background determines the detection limit, similarly to other characteristic X-ray analysis methods. The ingenuity has been exercised for increasing the detection capability or sensitivity; to increase the surface area irradiated by the probe beam by using a grazing angle incidence, and to reduce the bremsstrahlung background by making the analysis on photo-resist layers formed over the Si wafer for masking.

3.2. Experimental Procedure

3.2.1. Sample Preparation

Two-hundred-millimeter-diameter (200-mmϕ) p-type Si (100) wafers with a resistivity of 10 - 15 Ω·cm were used in this study. The photo-resist was chemical amplification type KrF resist that used Iodine (I) as Photoacid Generator (PAG). The thickness of the photo-resist after coating was 4.4 μm. The wafers were implanted with As, Ge and B ions using three kinds of ion implanters at ion energies ranging from 10 keV to 2 MeV with doses from 1×10^{12} to 5×10^{15} ions/cm^2. A batch-type high-current

implanter, a batch-type high-energy implanter and a single-wafer type medium current implanter were used for the measurement of dopant cross-contamination of a range of doses and energies.

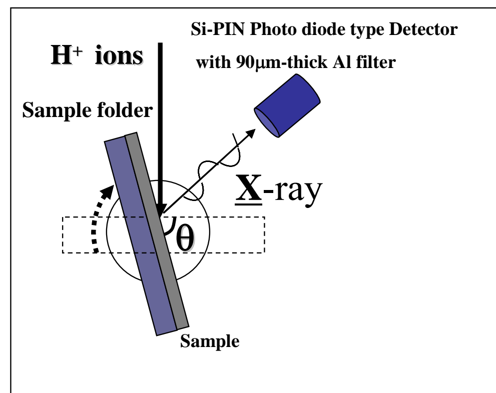

Fig. 3-1. Schematic of PIXE analysis system.

3.3.2. Experimental apparatus

A Tandem PELLETRON 5SDH-2 (National Electrostatic Corporation, USA) was used in this study as a source for 3.0-MeV proton probe beams [67]. Figure 3-1 shows a schematic of the PIXE analysis station. The Si-PIN photodiode type detector (XR-100CR) with 90-μm-thick Al filter is placed in front of a detector located at a detection angle of 135 deg. The probe beam is incident on the sample surface in which the axis of rotation lies, and the tilt angle, θ, was variable from 0 to 90 degrees.

3.3. Results and discussion

3.3.1. PIXE analysis with large tilt angle

PIXE can detect impurities of the depth of several ten μm from the sample surface because it uses a 3 MeV proton as a probe beam. However, to restrict the analysis to within a photo-resist layer that is only a few μm thick, grazing angle incidence PIXE is

needed.

Therefore, we performed PIXE analysis with a large tilt (incident) angle to increase the sensitivity to the ion implantation impurities by increasing the incident beam diameter on the sample. The As ions were implanted at an energy of 10 keV and a dose of 1×10^{14} ions/cm^2. A proton incidence of 10 μC at an energy of 3 MeV was used for each sample analysis. The proton beam diameter on the sample for normal incidence was 1 mm. The tilt angle was varied from 0 to 90 degrees in intervals of 0.5 degrees.

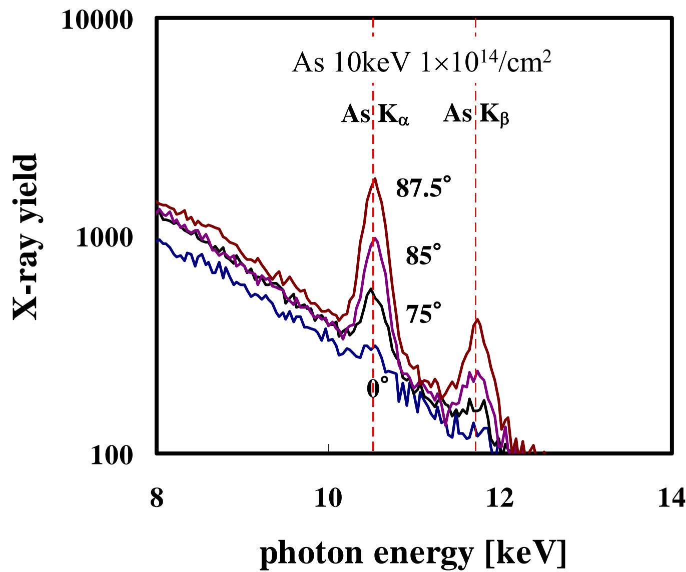

Fig. 3-2. Tilt angle dependence of the PIXE spectrum.

Figure 3-2 shows the tilt angle dependence of the measured spectrum. It shows that the K_α and K_β peaks of characteristic X-rays emitted from As atoms, which are of interest for analysis, grows as the tilt angle increases. The proton probe beam is projected as an ellipse on the surface of the sample by incidence with a large tilt angle, and its irradiation area increases in proportion to $1/\cos\theta$. Since As atoms are uniformly distributed laterally just near the sample surface by the ion implanter, as explained

below, it is expected that the peak yield increases proportionally to $1/\cos\theta$. This effect is equivalent to an increase in the effective path length through the implanted region, if the probe ions lose negligible energy during the transit.

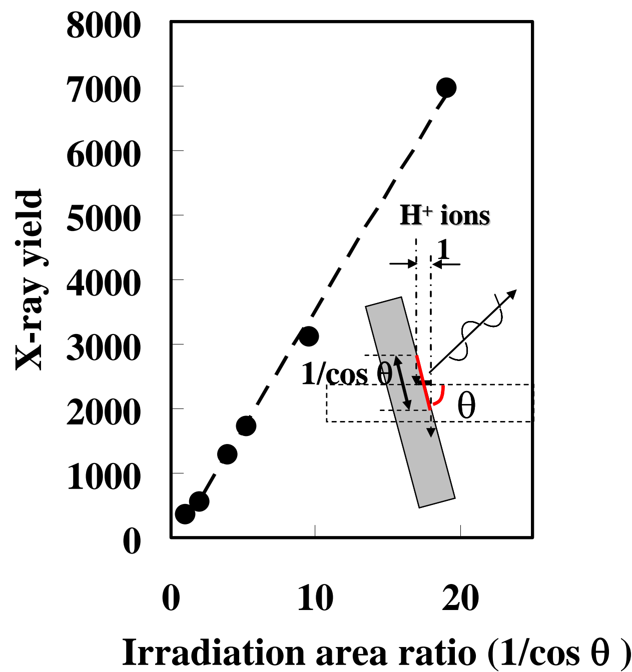

Fig. 3-3. Dependence of the Kα-X-ray yield of As on the tilt angleθ expressed in terms of the probe beam irradiation area.

From the measured peak intensity, the areal density of atoms of interest is calculated by using analytical software Gupixwin ver. 1.3. [68] Figure 3-3 shows the dependence of the As-K_α X ray yield on the probe beam incident angle θ. As has been expected, it is clearly shown that the yield increases just in proportion to $1/\cos\theta$, which is indicated by the broken line.

The projected range of 10-keV As ions in Si substrate is 0.026 μm, which is more than three-orders-of-magnitude smaller than the projected range of 3-MeV probe beam protons, *i.e.*, about 90 μm. The energy loss of the 3-MeV protons at 87-deg. incidence is

only about 12 keV during the passage through the As-deposited layer with thickness of about 0.5 μm (= 0.026 μm/cosθ). Since the X-ray emission cross-section varies very little for this energy difference in the As-deposited layer, the detected X-ray signal intensity is expected to be proportional to the areal density of As multiplied by the beam irradiation area.

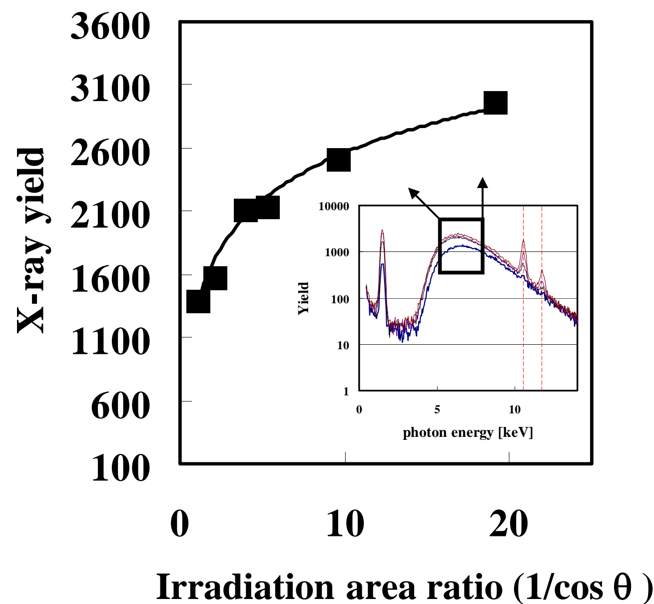

Fig. 3-4. Dependence of the peak height of bremsstrahlung continuum on irradiation area factor (1/cosθ).

The detection limit of impurities implanted in the Si substrate has been successfully lowered by a factor of about 20 in proportion to 1/cosθ. However, the use of grazing angle incidence increases not only the characteristic X rays emitted from impurities but also of the bremsstrahlung background emitted by secondary electrons, probe beam ions and recoil nuclei near the trajectory of the incident ions in the substrate, since the trajectory approaches the surface as the tilt angle increases, and therefore self-absorption of the X rays decreases. Figure3-4 shows the irradiation area (1/cosθ) dependence of the peak intensity of the bremsstrahlung background from the Si

substrate. It also increases as the tilt angle increases, and becomes at $\theta = 87$ deg. about twice as large as the value at 0 deg. Therefore, the improvement in the detection limit, or in the signal to noise (S/N) ratio, is only a factor of 10 (from 1×10^{14} /cm^2 improved to 1×10^{13} /cm^2), though the yield of the As K-X rays increases by a factor of 20.

3.3.2. Reduction of bremsstrahlung background by using photo-resist as an alternative low-Z surface for analysis

To reduce the bremsstrahlung background from the Si substrate, regions of the Si device wafers, which were covered with the photo-resist layer as a mask in the ion implantation process, were analyzed. Since I-line resist and the chemical amplification type KrF resist generally used in the ion implantation are composed mainly of low-*Z* elements, such as C, H, and O, and the bremstrahlung yield is proportional to Z^2, where Z is the atomic number of the atom in the target material, it can be expect that the background from resists is lower than that from Si. Since most of the wafer surface is covered with photo-resist when it is in the ion implantation process, sufficiently large area is usually available for the large tilt angle measurement.

Figure 3-5 shows the comparison of the PIXE spectra from two As-implanted Si samples; one with the photo-resist mask and the other bare Si substrate. The As ions were implanted at an energy of 10 keV and a dose of 5×10^{14} ions/cm^2. Since the projected range of the 10-keV As ions, R_p, is 23.3 nm in the photo-resist, and the film thickness of the photo-resist was 4.4 μm, all of the implanted As are stopped in the photo-resist. A 10-μC proton beam was used for the PIXE analysis at an energy of 3 MeV and a tilt angle of 87.5°.

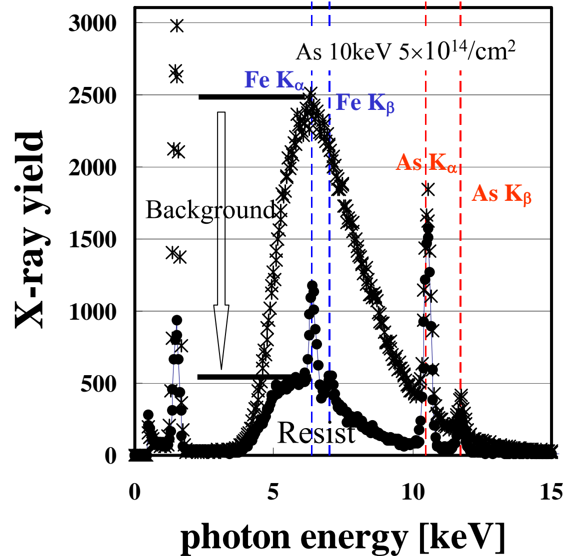

Fig. 3-5. Comparison of the PIXE spectra from samples implanted with 10-keV As ions at a fluence of 5×10^{14} cm^{-2}; bare Si (x), and photo-resist-covered Si (•). The tilt angle θ was 87.5 deg.

It is shown in Fig.3-5 that the bremsstrahlung background in the photon energy range from 3 keV to 12 keV is reduced in the case of the photo-resist to about 1/5 compared with that of the Si substrate, while the characteristic X rays remaining almost the same. That is, the S/N ratio is significantly improved, and the K_α and K_β peaks of implanted As are clearer.

In addition, another contaminant Fe, that was not able to be identified in the spectrum for the bare Si substrate, is clearly identified in the spectrum for the photo-resist-covered Si. The measured areal density of Fe, $\approx 5\text{x}10^{13}$ Fe/cm^2, is inconceivably large compared with that of the metallic contaminants typically seen in the modern ion implanters. Therefore, it is speculated that this contamination occurred during the preparation of the analysis samples, or that the Fe atoms are impurity atoms inherent in the photo-resist.

To clarify origins of these Fe levels, a number of unimplanted samples were analyzed. The levels of transition metals in these photo-resists were on the order of $1\times10^{11\text{-}13}$ atoms/cm^2 Fe, Ni, and Zn were detected. The volume metallic contamination specs of photo-resist solutions (solvent 90 %, solute10 %) are usually 10 ppb. This Fe level (up to10^{14} Fe per 10^{22} solute atoms) is consistent with the observed levels of Fe (up to $5\text{x}10^{13}$ Fe/cm^2) detected with our PIXE analysis.

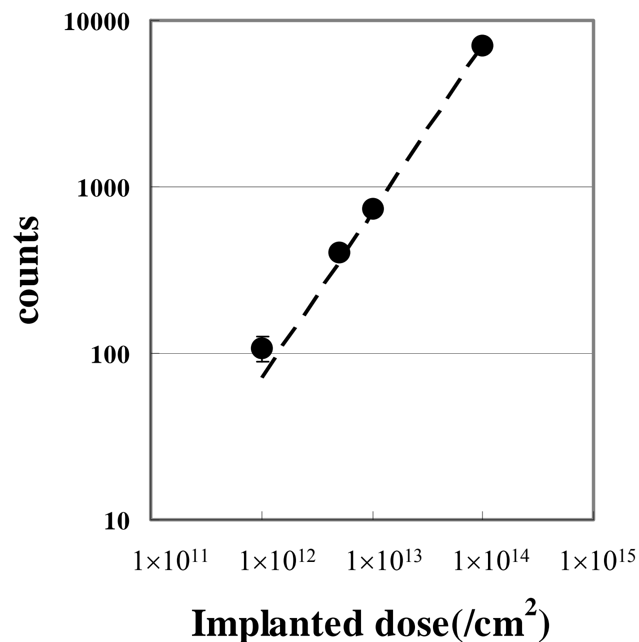

Fig. 3-6. Implantation dose dependence of the As-Kα X-ray yield from the photo-resist-covered Si. The tilt angle θ = 87 deg.

Figure. 3-6 shows the ion implantation dose dependence of the number of detected K_α-X rays of As measured by the PIXE analysis. A 3-MeV proton beam of 10 μC was used as the probe beam at the tilt angle of 87°. To decrease the uncertainty in various factors in the measurement system, the K_α-X ray of Iodine was used as an internal standard; *i.e.,* the number of detected X rays was normalized to that of Iodine K_α which is component of the Photoacid Generator (PAG) in the photo-resist. The volume density

of the photo-resist is taken as 8.57×10^{22} cm^{-3} for conversion into the areal density.

The ion implantation dose used as the abscissa is the time-integrated current, measured with the Faraday cup equipped in the ion implanter, divided by the implantation area on the sample target. The broken line represents a linear relationship between the dose and the X-ray yield. It is shown that the linearity holds for the dose as low as 1×10^{12} $/cm^2$ within an error of a factor of about 2. The growing disagreement near the dose of 1×10^{12} $/cm^2$ is due to the deteriorating signal-to-noise ratio. When the number of the probe beam protons was doubled to 20 μC, the S/N ratio was improved so that even the K_β-line was identified clearly. It can be expected that the detection sensitivity can be improved further by increasing the tilt angle of the sample, in proportion to $1/\cos\theta$, if the statistics is improved by increasing the probe beam fluence.

Depth distribution of the As implanted in the photo-resist is calculated by SRIM2008 [14] as shown in Figure 3-7. To measure the impurity ion implantation dose accurately, the depth distribution should not influence the measured X-ray yield. Differently from the sheet resistance metrology and the TW method, it can be expected that the measured value doesn't depend on the implantation depth or energy in the range below several MeV, because the X-ray emission cross section varies only by a factor of 0.7, when the proton energy decreases from 3 MeV to 2.6 MeV, as discussed below.

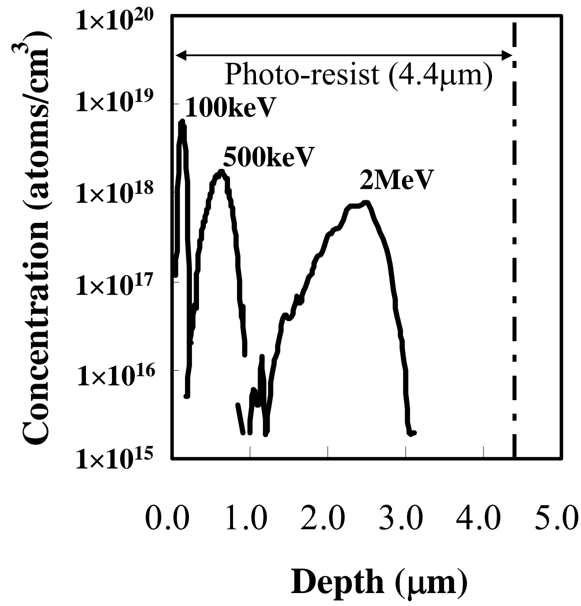

Fig. 3-7. Depth profiles of As atoms implanted into the photo-resist calculated by SRIM2008.

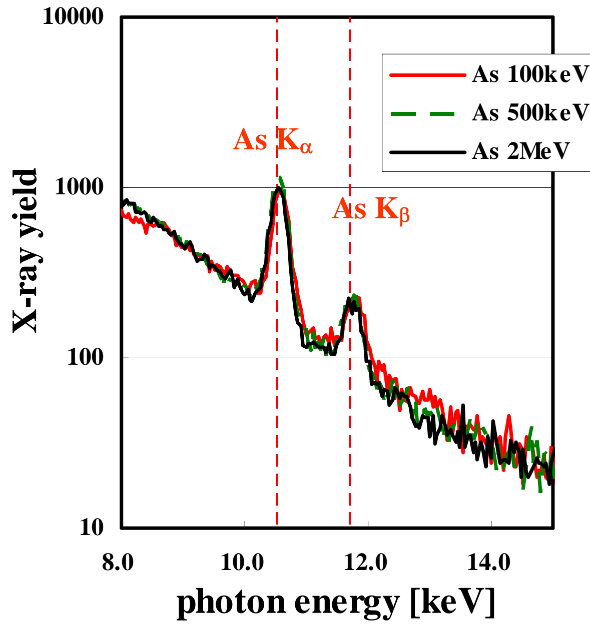

Fig. 3-8. PIXE spectra for 4.4 μm-thick photo-resist samples implanted with As ions, showing insensitivity to the ion energy.

Figure 3-8 shows the As ion energy dependence of the PIXE yield for As implanted

into the photo-resist. The tilt angle was set to 83 deg. with a dose of 5×10^{13} ions/cm^2 at an energy of 100 keV (the projected range R_p = 0.12 μm), 500 keV (R_p = 0.6 μm), and 2 MeV (R_p = 2.35 μm). The film thickness of the photo-resist was 4.4 μm, and the implanted As atoms are retained completely in the photo-resist as shown in Figure 3-7. At the distribution maxima, the energies of the probe beam protons incident with the tilt angle of 83 deg are 2.98 MeV, 2.90 MeV and 2.60 MeV, respectively. Accordingly, the K_α-X-ray emission cross section is decreased by 2 %, 8 %, and 28 %, respectively, at the distribution maxima. Since the X-ray yield is only weakly dependent on proton beam energy in the target, As signals were analyzed with an almost constant detection efficiency.

3.3.3. Evaluation of cross contamination

To demonstrate the effectiveness of the present method of sensitivity enhancement using the large tilt angle PIXE analysis on the photo-resist, a possible cross-contamination element that could be mixed while implanting the dopant atoms was evaluated. For these tests, a batch type high-current ion implantation machine was used for implantation of the sample covered with a 1.7-μm thick photo-resist layer. A 3-MeV proton beam incidence of 10 μC was used to analyze the sample at the tilt angle of 87°. In Figure 9 the solid line shows the measured PIXE spectrum for a sample implanted with a 10-keV ^{74}Ge ions (R_p = 23.3 nm in the photo-resist) at a dose of 2×10^{15} ions/cm^2. It had been taken just after finishing Ge ion implantation following the exchange of the ion species from As to Ge in the implanter ion source. The Ge implantation was made with a mass resolution $m/\Delta m$ = 50, which allows injection of ions with the mass ranging from 72.52 u - 75.48 u. We notice existence of a small peak at the As-K_α line, which means cross-contamination of ^{75}As. By normalizing the peak

intensity to that of Ge, the areal density of As is found to be approximately 1.79×10^{13} $/cm^2$ (statistical error 7.21 %, minimum limit 1.9×10^{12} $/cm^2$). Therefore, it has been found that the cross-contamination of As occurs at an areal density two orders of magnitude lower than the implantation dose of Ge, and that the minimum limit of detection is 1.0×10^{12} $/cm^2$ in spite of large peaks of Ge-K_α and Ge-K_β. It should be noted that it is difficult to identify the contaminant ^{75}As by SIMS analysis because of possible interference by ^{74}GeH.

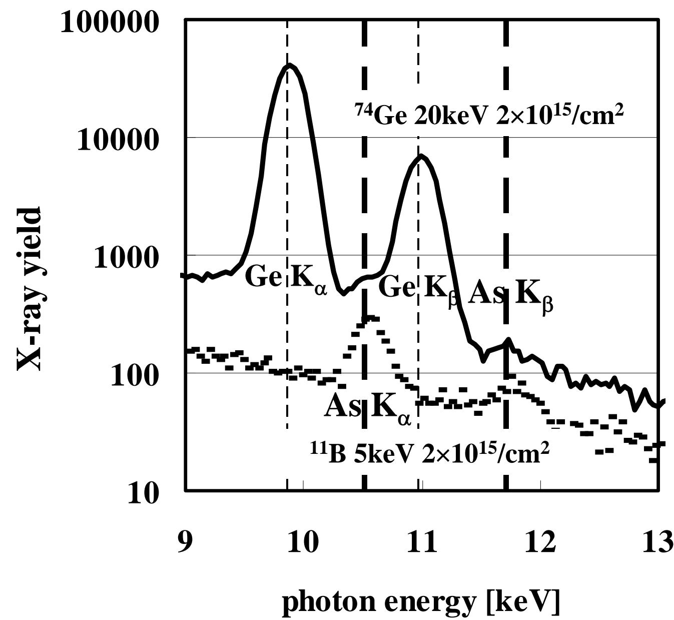

Fig. 3-9. PIXE spectra just after implantation with Ge (solid line) and with B (dashed line). Peaks at As-K lines indicates occurrence of cross-contamination.

The short dashed line is a spectrum showing cross-contamination of As during B ion implantation at a dose of 1×10^{15} $/cm^2$ into another wafer with the same implanter just after As ion implantation at a dose of $1\times10^{16}/cm^2$. The cross-contamination of As at an areal density of 1.43×10^{13} $/cm^2$, which is two orders of magnitude lower than the dose of B, was identified, similar to the case of Ge.

Usefulness of cross-contamination monitoring is demonstrated also for *in situ* cleaning of the system. The cleaning time dependence of the areal density of the cross-contaminant on the wafer surface during the beam line cleaning with an Ar ion beam is shown in Figure 3-10. The areal density of the cross-contaminant As decreases exponentially with a decay time constant of 35 min as the Ar cleaning time increases. It should be noted in practical application that the As cross-contamination of about 0.5% of the B dose remained still after 30 minutes of Ar cleaning. Recently active beamline cleaning techniques have been developed, using XeF_2 and other chemistries, which are more efficient in removing dopant and other contaminants from implant beamlines [69].

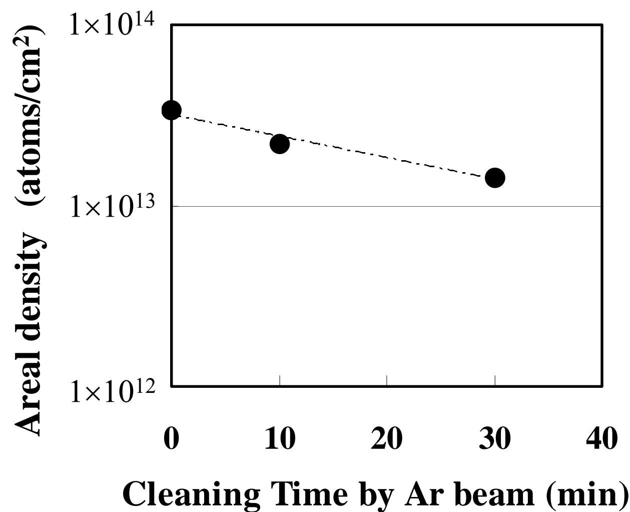

Fig. 3-10. Dependence of the areal density of the cross-contaminant on Ar ion beam cleaning time.

3.4. Conclusion

Two improvements in the use of PIXE analysis are described here for detection of cross-contamination in high-dose implants, (1) the use of grazing angle proton beam incidence on the wafer surface and (2) the collection of data from un-patterned regions of the photo resist mask layer to reduce the bremsstrahlung background levels. The

combination of these two improvements lowered the detection level for As to 10^{12} As/cm^2. The use of this improved PIXE method was confirmed in the detection of As cross-contaminants in high-dose B and Ge implants. It is expected that the success of this use of PIXE analysis for detection of low-level surface contaminants will encourage the development of compact proton accelerators for use as in-line process evaluation tools using grazing angle PIXE analysis.

Chapter 4. Charging phenomena during medium current ion implantation of carbonized photo-resist surface layers

4.1. Introduction

In ion implantation, one of the indispensable technologies in the semiconductor device manufacturing process, electrostatic charging phenomenon has been one of the most serious problems. Charging phenomenon is widely considered to be a problem that is limited to high current ion implantation. Therefore, the researches so far have been mainly carried out in the high current range, i.e., the beam current of the order of 10 mA and the dose greater than 1×10^{14} /cm^2 [71, 72], and there are some popular methods for characterization. As a result of extensive researches, [73, 74, 75], ion implanters in recent years are often equipped with a plasma flood gun (PFG) [76] that supplies electrons and ions to neutralize the positive charge brought by the ion beam itself and by secondary electrons emitted from the wafer surface. However, because of the propagation of system LSI, it is demanded to construct a large number of small-scale transistors with different functions in one chip. Therefore, the necessity for implanting the ions with a photo-resist mask having much more complex structure has arisen. As a result, charging phenomenon has come to be observed also in the medium current implantation machines with the beam current smaller than several hundred μA and implanting doses smaller than 5×10^{13} /cm^2 which obliges medium current ion implantation machines to also be equipped with a PFG. It is difficult for conventional characterization tools, such as MOS capacitors with charging collecting electrodes, etc., to detect these phenomena, and the mechanism is not yet clarified. Figure4-1 shows a

typical result of the wafer charging phenomenon in a medium current ion implanter. The charging phenomenon in the medium current range strongly depends on the aperture of the mask, or the area ratio of the aperture and the mask area, and the mask pattern arrangement of the chips. We also notice a strong dependence on the chemical composition of the photo-resist

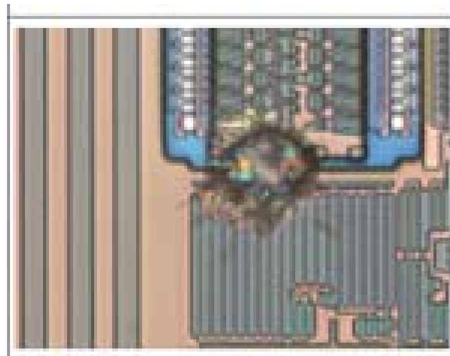

Fig. 4-1. A typical result of the wafer charging phenomenon in a medium current ion implanter.

Similarly to the wafer charging phenomenon, research on the interaction of implanted ions and the photo-resist has been done primarily only in the high dose range. It has been said that implanted impurities become cores of the cross-linking reaction which induces formation of the carbonized layer on the surface of the photo-resist [77, 78]. Most of current researches discuss the photo-resist surface completely carbonized by the ion implantation and the removal method of the carbonized layer [79, 80, 81]. Because the carbonized layer formed on the photo-resist surface by the ion implantation can not be dissolved in strongly acidic solutions, e.g., HF solution, for chemical analysis, examination of the mechanism of quality change is extremely difficult. In addition, the photo- resist used for a mask of the ion implantation is required to have increasingly high resolution as in the case of microfabrication like dry etching, etc., i-line photo-resist tends to be replaced by KrF photo-resist. These conditions make the

mechanism of the quality change more complex.

In the present work, to examine charging phenomenon in medium current implanters, the potential on the surface of the wafer immediately after ion implantation has been measured for the first time with a surface potential measurement tool based on an electrostatic voltmeter. The carbonized layer on the surface of the photo-resist is analyzed by using a TOF-SIMS analysis method [82]. Moreover, the thickness of the carbonized layer is measured with a Surface And Interfacial Cutting Analysis System (SAICAS) [83], and the relation in the medium current implantation regime between the thickness and the ion implantation condition is discussed to investigate the relation between change in photo-resist quality and wafer charging phenomenon.

4.2. Experimental Procedure

Two-hundred-millimeter-diameter p-type Si (100) wafers with a resistivity of 10 - 15 Ω·cm were used in this study. The photo-resists used were several kinds of the chemical-amplification-type KrF resist and the i-line resist. The thickness of the photo-resist after coating was around 1.0 μm. The wafers were implanted with As, P and B ions using a single-wafer-type medium current implanter at ion energies ranging from 9 keV to 50 keV with doses from 1×10^{13} to 5×10^{15} ions/cm^2.

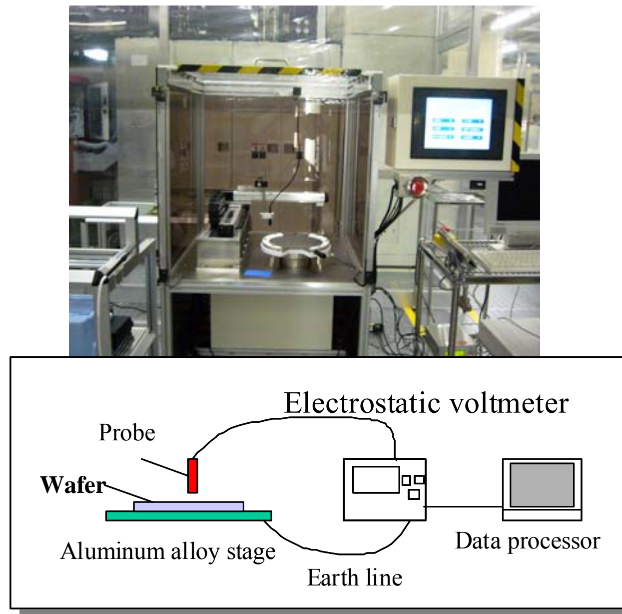

Fig. 4-2. A schematic diagram of the surface potential measurement system.

A schematic diagram of the surface potential measurement system is illustrated in Figure 4-2. An electrostatic voltmeter (TREC: MODEL541) [84] is used in this system and the back side of the wafer under measurement are connected to the machine ground. The distance of the surface of the wafer and the probe tip is always kept 1mm, and in order to scan accurately on the wafer at intervals of 2 mm, the probe is fixed by an automatic transportation arm. The lateral resolution is a circular region with about a 5 mm diameter. Information on the measurement position and the measured value of the potential is saved in a control computer automatically. SAICAS (DATPLA WINTES Co. Ltd., : DN-20) and TOF-SIMS (Physical Electronics: TRIFT-2) were used to analyze the carbonized layer on the surface of the photo-resist.

4.3. Results and Discussions

4.3.1. Relations between carbonized layer and implanted impurities

First, SEM measurements were done to examine dose dependence of the formation

of the deformed or transformed layer. Figure4-3 shows the SEM cross-section images after removal processing by isoamil acetate. A layer of some transformed material at the surface of the photo-resist is observed when the ion dose is equal to or greater than 1×10^{14} /cm^2. This layer is difficult to remove as has already been reported [71]. However, it is confirmed that a thin film of the degenerated photo-resist residue was formed even at the dose smaller than $1x10^{13}$ /cm^2 as is seen in the uppermost image in Fig. 4-3.

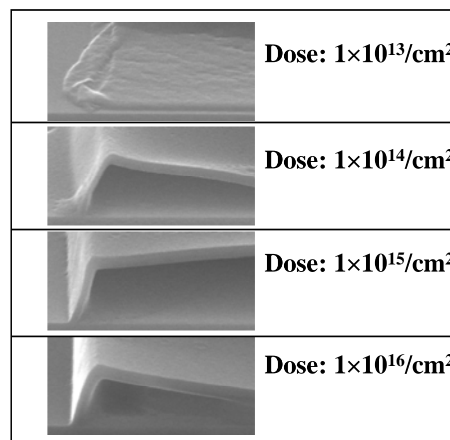

Fig. 4-3. The SEM cross-section images after removal processing by isoamil acetate. The P ions were implanted at an energy of 50 keV.

In order to clarify the process of quality change, the surface of the high-dose implanted photo-resist was cut off with a slope of 1/1000 by the SAICAS method, and the ground surface was analyzed by TOF-SIMS. Figure 4-4 shows an example of the image of the SAICAS-applied surface. The P ions were implanted at an energy of 50 keV and a dose of 5×10^{15} ions/cm^2. As for the non-implanted sample, cutting-off with a desired slope was possible everywhere on the photo-resist. However, the ion implanted sample did not allow cutting-off with such an extremely grazing angle. A step with a height of about 100 nm was created on the surface, as shown in Fig. 4-4(a). Cutting-off at the desired slope was possible only for the deeper portion of the bulk resist. It is

inferred that this phenomenon is linked to the presence of the carbonized layer that was hardened by the ion implantation. So, these samples were divided into five areas (Table 4-1), and were analyzed by TOF-SIMS (primary ion= Ga, energy= 15keV) independently.

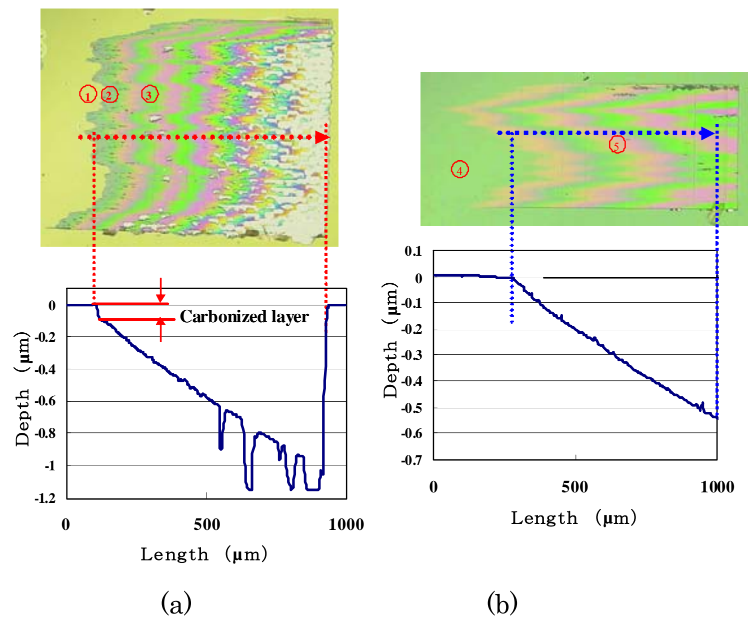

(a) (b)

Fig. 4-4. The example of the image of the SAICAS-applied surface. (a) Implanted sample The P ions were implanted at an energy of 50 keV and a dose of 5×10^{15} ions/cm^2. (b) Non-implanted sample.

TABLE 4-I

Measurement point 1	Implanted	surface (P)
Measurement point 2	Implanted	on the ground surface at 100 nm from the original surface
Measurement point 3	Implanted	on the ground surface at 250 nm from the original surface
Measurement point 4	Non	a virgin surface
Measurement point 5	Non	an arbitrary point on the ground surface

Figure 4-5 shows comparison of the ion intensity ratio measured by TOF-SIMS.

The ion intensity ratio was normalized to the intensity of carbon. The implanted P exists only in the measurement point 1. However, the signal related to the P-C bond, that could indicate that the implant P were a core of the cross-linking reaction, was not detected at all. Instead, the signal related to the P-O bond was detected definitely. This implies that the carbonized layer is formed as a result of the cross-linking reaction, the cores of which are not the implanted impurities themselves, but the bases containing the impurity and oxygen atoms in the photo-resist.

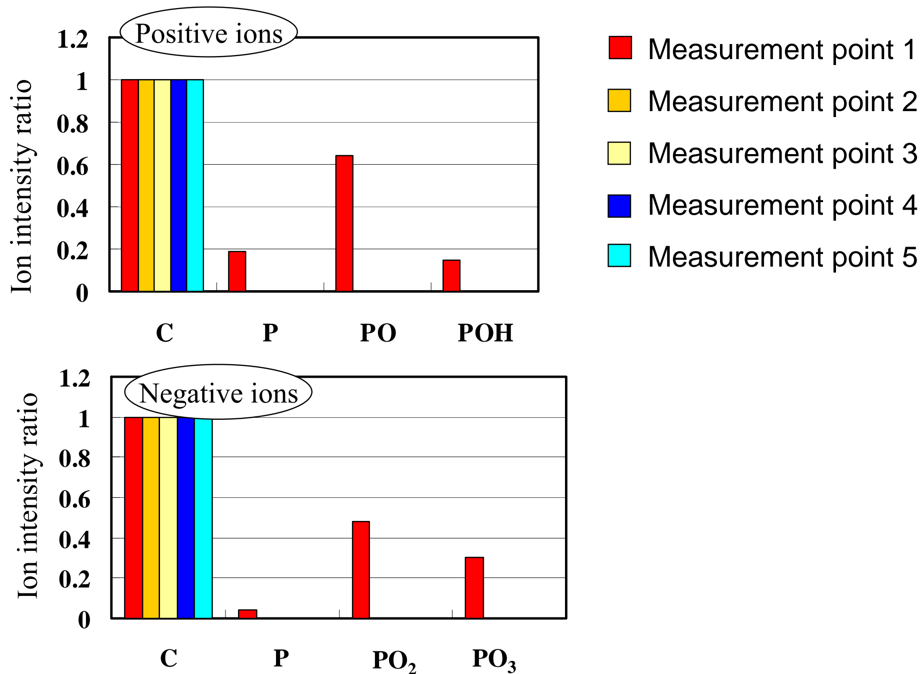

Fig. 4-5. Comparison of the ion intensity ratio measured by TOF-SIMS.

4.3.2. Thickness of carbonized layer

Dependence of the thickness of the carbonized layer on the implantation energy is examined. The thickness was deduced from the above-mentioned step created by application of SAICAS, as explained in the following.

First of all, 9-keV boron ions, 25-keV phosphorus ions and 42-keV arsenic ions were implanted with the same dose of 5×10^{15} /cm^2. They all have the same stopping range R_p (= 65 nm) in the photo-resist on the Si wafer. They are then processed by the SAICAS method, and the step height is measured. The data were taken at 20 points on every sample averaged to have the thickness of the carbonized layer.

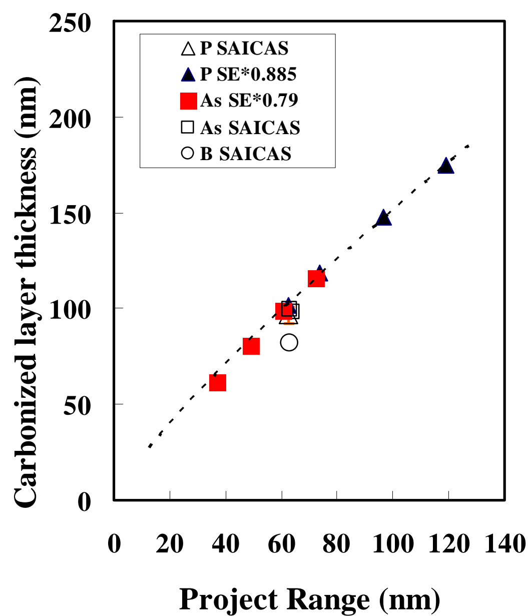

Fig. 4-6. The energy dependence of the carbonized layer thickness was examined by implantation of P and As. Tc is plotted as a function of Rp.

Next, the photo-resist film thickness is measured by the spectroscopic ellipsometry (SE) both for the implanted sample and a non-implanted one. The implanted photo-resist is divided into two regions; the carbonized surface layer and the unaffected rest. It is difficult to construct any model to evaluate the carbonized layer by SE. Therefore, only the unaffected photo-resist layer thickness were taken into account; subtracting this thickness from the initial film thickness, a temporary value were obtained for the carbonized layer thickness. Comparing the temporary value with the

carbonized layer thickness determined with SAICAS, the ratio is calculated to define a shrinking percentage. The shrinking percentages, F_s, thus calculated are 1.0 for B, 0.885 for P, and 0.790 for As, respectively, and corrects phenomenologically for combined effects of the implant range straggling and those related to SE; The carbonized layer thickness, T_c, is calculated from the initial thickness, T_i, and the SE thickness, T_{SE}, by a relation; $T_c = F_s \cdot (T_i - T_{SE})$.

The energy dependence of the carbonized layer thickness was examined by implantation of P and As that have large shrinkage percentages. The P and As ions were implanted at an energy of 25 - 50 keV, and 20 - 50keV, respectively, and a dose of 5×10^{15} ions/cm^2. Figure 4-6 shows the result, where T_c is plotted as a function of R_p. The carbonization layer film thickness increases basically almost proportionally to R_p with a slight dependence on the ionic species. This is a firm evidence for the contribution of the stopping power of the photo-resist to the formation mechanism of the carbonized layer. It is inferred that the molecular bond is cleaved by the kinetic energy of implant ions which are incorporated to the photo-resist molecules to form mainly oxide groups, and the cross-linking reactions develop afterwards. The amount of the cross-linking reaction increases with the implantation dose until the carbonized layer is formed.

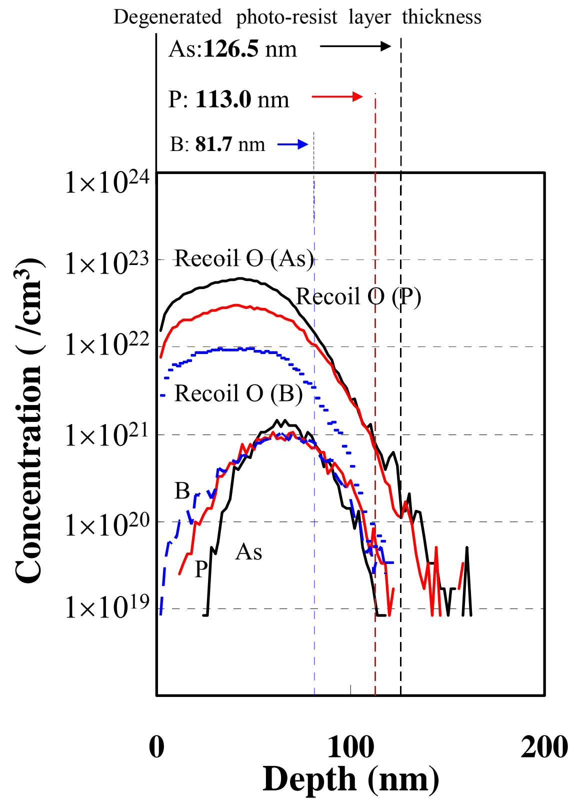

Fig. 4-7. Depth distributions of the implant ions and the recoil oxygen atoms using by SRIM2008. The photo-resist density of 0.95 g/cm3 and the stoichiometry of 'C:H:O=5:8:2' were used in the calculation.

In order to clarify the relation between the implantation condition and the carbonized layer thickness, a simulation software SRIM2008 [85] was used. The result of the simulation for the relevant ions are shown in Fig. 4-7, where depth distributions of the implant ions and the recoil oxygen atoms in the photo-resist are shown for the implant dose of 5×10^{15} /cm^2. The degenerated layer thicknesses (*Ti-Tse*) obtained as mentioned above are also indicated in the figure. It is found that the carbonization takes place in the region with recoil oxygen densities greater than 3×10^{21} /cm^3, 6×10^{20} /cm^3 and 1×10^{20} /cm^3, for B, P and As, respectively. These values are considered to be the critical values for carbonization.

It is then possible to hypothesize that the sample begins to be carbonized when the maximum Oxygen recoil density reaches the critical density. Since the peak density of the recoil Oxygen increases proportionally to the implant ion dose, it is inferred that the critical dose, at which the carbonization begins to take place at the depth of maximum oxygen density, is 1.5×10^{15} /cm^2 for B, 8×10^{13} /cm^2 for P and 1×10^{13} /cm^2 for As. It should be noted that the carbonization by P and As takes place in the medium current implantation regime, i.e., the dose $\leq 1 \times 10^{14}$ /cm^2, while B has a high critical dose exceeding 1×10^{15} /cm^2.

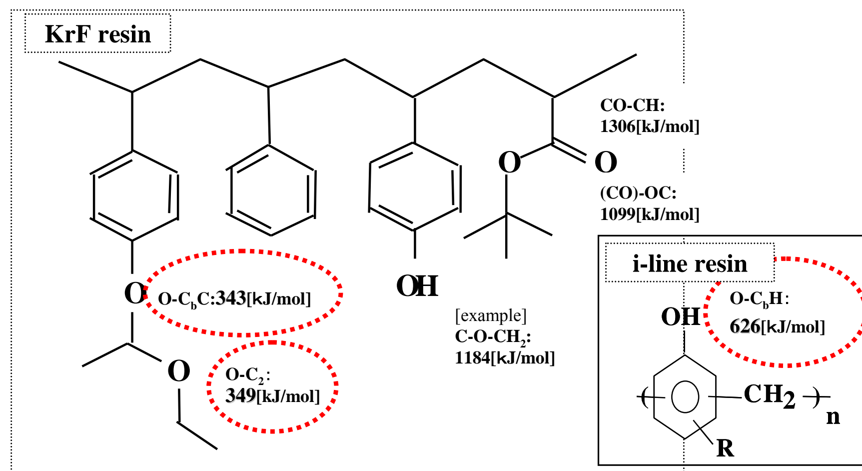

Fig. 4-8. Schematic diagrams of molecular configurations and some bond energies of the photo-resists.

4.3.3. Mechanism of the carbonized layer formation

Next we examine deterioration of the removal performance due to the formation of the carbonized layer on the surface of the photo-resist. Molecular configurations and some bond energies of the photo-resists are schematically shown in Fig. 4-8. It should be noted that every segment with the minimum bond energy has an oxygen atom, regardless of the kind of the photo-resist.

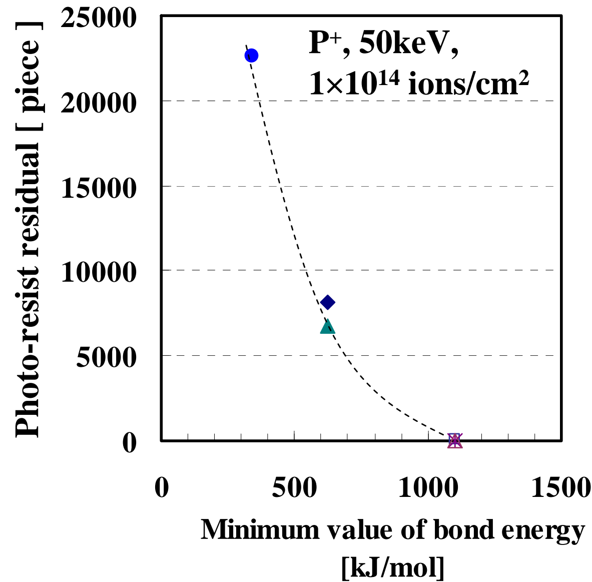

Fig. 4-9. The number of the photo-resist residuals was measured by wafer surface and dark field defect inspection system, is plotted against the minimum bond energy. The minimum defect size is 0. 1 μm.

Phosphorous ions were implanted at an energy of 50 keV and a dose of 1×10^{14} ions/cm^2 into three kinds photo-resist of the photo-resist with different bond energy [86]; the i-line photo-resist, the acetalic KrF acrylic photo-resist, and the acrylic KrF photo-resist. The number of the photo-resist residuals, measured by a wafer surface dark field defect inspection system, is plotted against the minimum bond energy in Fig.4-9. The amount of the photo-resist residuals increases with decreasing minimum bond energy. It is inferred that the mechanism of carbonized layer formation on the photo-resist surface by ion implantation can be as follows. The molecular bonds of the photo-resist are cleaved by the energy of the implanted impurities most abundantly at the segments with the smallest bond energy, which contain oxygen without exception. At these radicals oxygen pickup reactions by the implant phosphor atoms occur as well

as the cross-linking reactions. Thus losing the oxygen and Hydrogen atoms, the carbon-rich layer is formed to finally become the carbonized layer. The photo-resist materials with lower minimum bond energy are apt to form the deteriorated layer more easily. Recently, the degree of integration and performance required for semiconductors are becoming more and higher, and accordingly the photo-resists material has to be more and more sensitive and reactive, which makes the bond energy of the candidate material lower and lower. KrF photo-resists need higher resolution than i-line photo-resists, and so the minimum bond energy is lower. This difference in the minimum bond energy should be the reason for the difference in the threshold dose for the deteriorated layer formation between KrF and i-line photo-resists.

4.3.4. Surface potential of the wafer and discharge

The photo-resist is a complete insulator before the ion implantation. However, when the carbonized layer is formed, it is considered that the surface is changed into a conductor. Therefore, there are possibilities that this conversion of the photo-resist surface affects the charging phenomenon during the ion implantation. Then, a capacitor model is developed here to treat the problem quantitatively. As is well known, the electrostatic capacitance C_m of a dielectric film with an area of S and a thickness of d_m sandwiched between two electrodes is expressed as follows;

$$C_\mathrm{m} = \varepsilon_\mathrm{m}\varepsilon_0 \frac{S}{d_\mathrm{m}}, \tag{4-1}$$

where ε_0 and ε_m is the permittivity of free space and the relative permittivity of the film material, respectively. In our typical case of the Si wafer covered with a layer of 0.4-µm-thick silica ($\varepsilon_{\mathrm{SiO2}}$ = 4.2) and that covered with a 1-µm-thick photo-resist film (ε_res = 3.0), with a carbonized layer on the top of the photo-resist, C_{SiO2}/S = 9.3 nF/cm^2

and C_{res}/S = 2.7 nF/cm^2. For the portion covered with both the layer and the film, the formula for the series connection of the capacitors as applied to have $C_{SiO2+res}/S$ = 2.1 nF/cm^2. Then the surface potential induced by ion implantation can be calculated from,

$$V_{m} = \frac{Q}{C_{m}} = \frac{Q/S}{C_{m}/S}, \qquad (4\text{-}2)$$

where Q = eFS is the charge introduced by the implantation up to a dose of F [/cm^2]. From the values evaluated above, it is expect that V_{SiO2} =170 V, V_{res} = 600 V and $V_{SiO2+res}$ =780 V for a dose F = 1 × 10^{13} cm^{-2}.

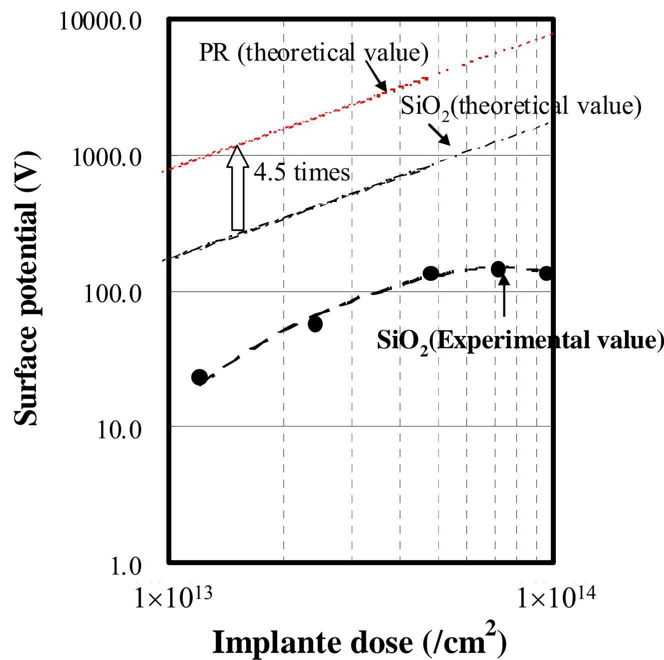

Fig. 4-10. The surface potential was measured for the Si wafer with the above mentioned geometry implanted with 40-keV P ions at a current of 100 μA up to a dose of 1 × 10^{13}- 1 × 10^{14} ions/cm^2 by using a single-wafer type medium current implanter.

The surface potential was measured for the Si wafer with the above mentioned

geometry implanted with 40-keV P ions at a current of 100 μA up for a dose of 1×10^{13}-1×10^{14} ions/cm^2. A single-wafer type medium current implanter was used, which is equipped with a suppressor for the secondary electrons from the surrounding of the wafer (without a PFG system). The results are shown in Fig. 4-10, where V_m calculated from Eq. (4-1) and Eq. (4-2) is expressed as the thin broken line. The surface potential increases linearly with the implantation dose up to 5×10^{13} cm^{-2}, and saturates at about 150 V. However, the absolute values are lower than the theoretical values V_{th} by a factor of 5.7. Since a PFG is not used in the present implanter, the discrepancy should be due to incomplete suppression of incidence of electrons carried by the ion beam and those emitted from peripheral structural components. The surface potential of the SiO_2 film reaches its maximum value of about 150 V at the dose of 6×10^{13} cm^{-2}, and begins to decrease for the higher dose. This is considered to be due to leakage or breakdown. The experimental value of the saturation field of 150 V divided by 400 nm is smaller than theoretical value, which is due to the effects of the implanted ions; introduction of foreign atoms, introduction of charge, and damage along the implanted ion paths. This phenomenon also is due to the effects of the electrons: transported with ion beam, and the secondary electron supplied to the wafer by a peripheral equipment component.

If the surface potential exceeds 150 V, the electric charges on the oxide film should leak out and the surface potential would decrease.

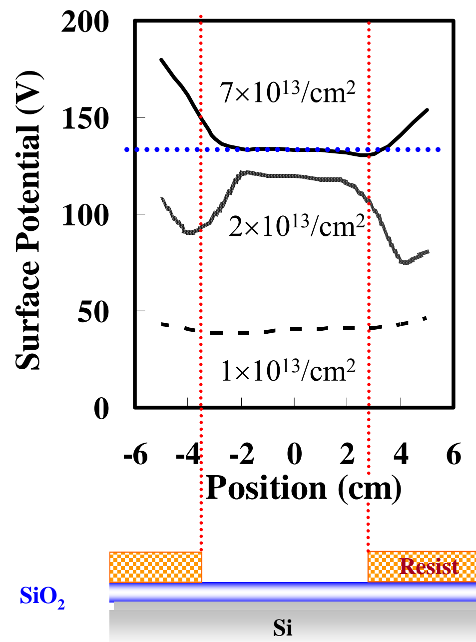

Fig. 4-11. The surface potential distribution measured for different doses of implantation. A 400-nm-thick SiO_2 covered wafer, which has a 1-µm-thick i-line photo-resist coating with a 360-mm^2 square opening, was used.

Next, a 400-nm-thick SiO_2 covered wafer, which has a 1-µm-thick i-line photo-resist coating with a 360-mm^2 square opening, was prepared to examine the dose dependence of the voltage distribution on the implanted surface. Figure 4-11 shows the surface potential distribution measured for different doses of implantation. At the dose of 1×10^{13} /cm^2, the surface potential is almost constant over the wafer, irrespective of the pattern of the photo-resist on the SiO_2. This is considered to be a result of charge neutralization by stray electrons which rush into the photo-resist surface, which otherwise might have had a very large potential as mentioned above, and possibly resulted in discharge.

When the dose is increased to 2×10^{13} cm^{-2}, the potential approaches the critical

value of 150 V for the charge leakage or the breakdown. The nonlinear three-fold increase with two-fold increase in the dose means a deficiency of the stray electrons in the surrounding space. The dips at the boundary might suggest that the breakdown or the leakage is easier to take place at the material boundary.

At doses well above this dose, the accumulated charge makes the potential greater than 150 V everywhere, as is seen in the case of the dose of 7×10^{13} cm^{-2}. However, the potential on the SiO_2 film cannot exceed the critical value of 150 V, at which the SiO_2 film start to be degraded and the charges on the surface begin to leak as has been shown in Fig. 4-10. The dose 7×10^{13} cm^{-2} is nearly equal to the critical dose of P (8×10^{13} cm^{-2}) for carbonization. Therefore, it is thought that an almost completely carbonized layer is formed on the surface of the photo-resist at this stage. The increased mobility of the charge on the carbonized layer does not allow for the potential on the photo-resist surface to grow much greater than that on the SiO_2 surface. The carbonized layer on the photo-resist is then considered to play a role of a collector of the charges that flow into the SiO_2 region and are discharged mainly at the boundary.

Thus, it has been shown that, even in the machines with the low beam current of the order of 100 μA, the photo-resist plays the role of a capacitor or a charge collector, which supplies the accumulated charge through the carbonized layer into the open area, and induces leakage or breakdown at relatively low dose of the order of 10^{13} ions/cm^2.

4.3.5 Consequences of the charging phenomena in actual devices

Figure 4-12 shows the surface potentials for KrF photo-resist compared with those of i-line photo-resist. In the case of the KrF photo-resist, the electric charges flow onto the open SiO_2 area at the dose as low as $1x10^{13}$ cm^{-2}, while no charge flow is observed for the i-line photo-resist. The reason is as follows; at the surface of the KrF photo-resist

with lower minimum bond energy the carbonized layer is more easily formed, which allow the electric charges to flow onto the SiO_2 film even at the low implantation dose.

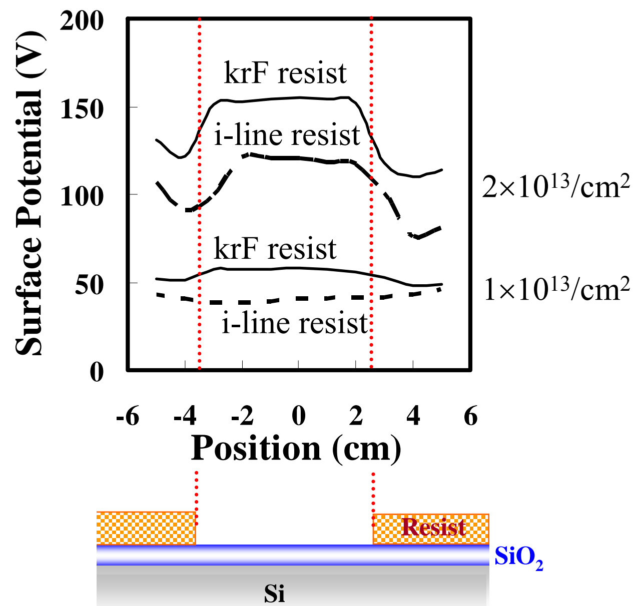

Fig. 4-12. The surface potentials for KrF photo-resist compared with those of i-line photo-resist. Ion implantation was done with P ions at an energy of 40 keV.

Next, a sample was prepared that has a structure similar to the actual device, and ion implantation was done with P ions at an energy of 40 keV up to a dose of 1.8×10^{13} cm^{-2}. The thickness of the oxide film is about 10 nm, and shallow trench isolation (STI) has a thickness of about 400 nm. The surface potential distribution is shown in Fig. 4-13. Five steps corresponding to five regions with different permittivity in the potential distribution can be recognized. As is supposed from eq. (4-1) and (4-2), the height of the steps increases with decreasing capacitance except on the STI. This exception clearly shows that the accumulated charge in the photo-resist region is flowing into the uncovered SiO_2 region through the STI region, which increases the charge on the STI to

raise the potential there, and a potential difference of about 130 V is established across the boundary between the thin oxide film. Because the electric field strength, induced by a 130 V difference across the transient region of about 3 nm thickness as seen in the figure, would exceed several hundred MV/cm, it is easily supposed that the explosion-like discharge as shown in Fig. 4-1 is triggered.

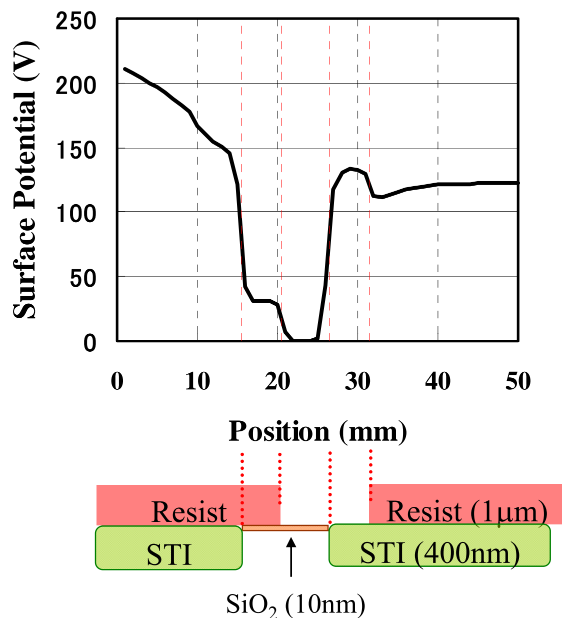

Fig. 4-13. The surface potential distribution of a sample having a structure similar to the actual device. Ion implantation was done with P ions at an energy of 40 keV up to a dose of 1.8×10^{13} cm^{-2}. The thickness of the oxide film is about 10 nm, and shallow trench isolation (STI) has a thickness of about 400 nm.

The surface potential increases with decreasing area of the uncovered region as is shown in Fig. 4-14. For this measurement, As ions were implanted at an energy of 30 keV up to a dose of 2×10^{13} ions/cm^2 into a 400-nm-thick SiO_2 film on a Si wafer with the KrF photo-resist coating. Extrapolating the dependence to the actual dimension of

the devices, we can easily assume much smaller threshold dose for the explosive discharge.

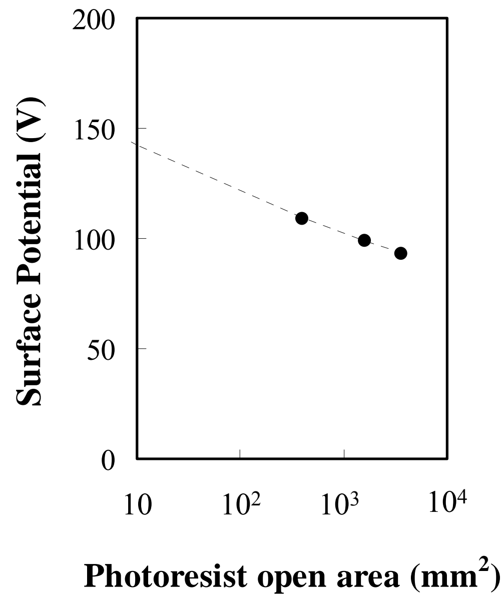

Fig. 4-14. The surface potential increases with decreasing area of the uncovered region.

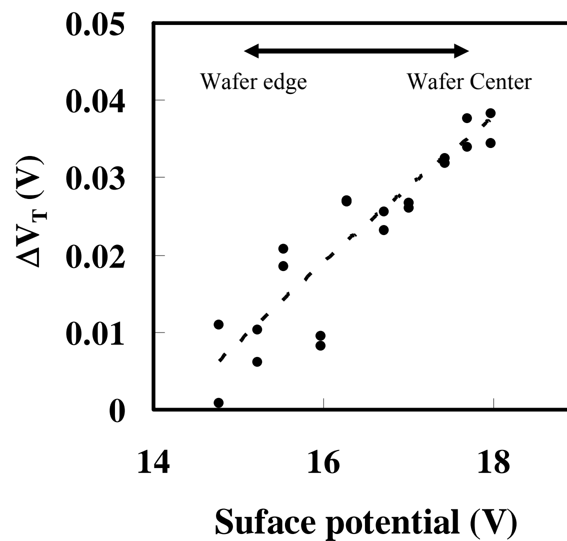

Fig. 4-15. The voltage shift ΔV_t increasing in proportion to the surface potential caused by the ion implantation.

The rapid rise of the surface potential would induce unexpected influence in an actual device. One is the phenomenon of threshold voltage shift in N-channel transistors. Figure 4-15 shows the voltage shift ΔV_t increasing in proportion to the surface potential caused by the ion implantation. A schematic of the transistor is shown in Fig. 4-16. In this case, the open area has a dimension of 1 μm x 1 μm, and the most of the open area is occupied by the STI with a 400-nm depth. Into the pocket 70-keV/100-μA B ions were implanted up to a dose of 4×10^{12} cm^{-2} successively after 30-keV /250-μA P ions were implanted up to a dose of 4×10^{13} cm^{-2} into the extension. The value ΔV_t is the difference in the threshold voltage V_t between those without and with the PFG in the process of the extension P implantation. In all other processes, they were treated similarly.

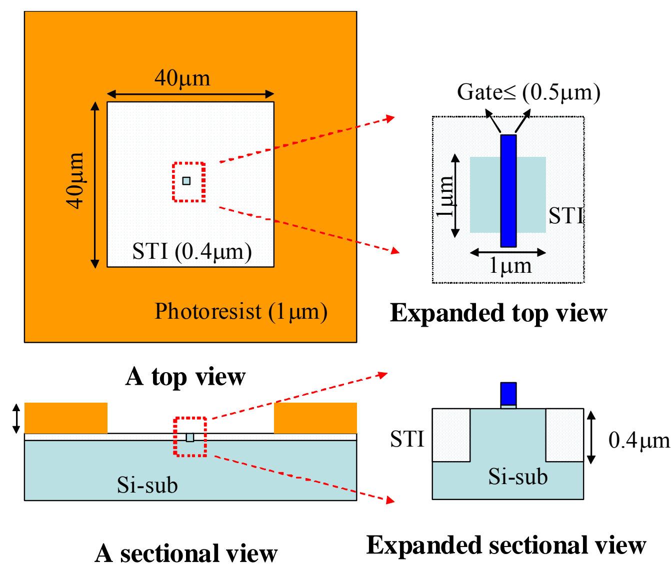

Fig. 4-16. A schematic of the transistor. The open area has a dimension of 1 μm x 1 μm, and the most of the open area is occupied by the STI with a 400-nm depth.

In general, the surface potential at the middle of the wafer is high compared with the peripheral region. This is because the secondary electrons are supplied from the

edge-cut part with about 5-mm width in the outermost part of the wafer. Since the lateral resolution of the electrostatic voltmeter probe is 5 mm, the measured values are the mean values averaged over the surrounding area, and are lower than the maximum value. It is easily supposed from the result of Fig. 4-16 that the surface potential would exceed several hundred volts in the relevant area after the extension P implantation The surface potential rise affects the B beam pocket implantation through changes in the incident angle, current density, etc, which would induce an under-dose phenomenon.

It is easily supposed that phenomena similar to the above-mentioned case will take place more frequently, as the tendency to replace the devices by system LSIs is further developed from now on. Consequently, there will be increased necessity to cope with the pattern-effects in medium current ion implantation machines that have not been the problems up to now.

4.4. Conclusion

Formation of the carbonized layer takes place in the medium current ion implantation machines on the surface of the photo-resist even at relatively low doses, of the order of 1 x 10^{13} ions/cm^2. The molecular bonds of the photo-resist are cleaved by the kinetic energy of the implanted impurities mainly at the portions containing oxygen with the smaller bond energy, where oxygen pick-up reaction by the implant ions and cross-linking begins to take place, and the carbonized layer is finally formed. This means that the photo-resist materials with lower minimum bond energy are more likely to form a carbonized layer.

When the carbonized layer is formed on the surface of the photo-resist, it plays the role of a capacitor, which transfers the accumulated charge to the open area, which

induces a large electric field at the STI, for example, often resulting in damaging discharges. It is easily supposed that phenomena similar to the above-mentioned case will take place more frequently, as the tendency to replace the devices by LSIs is further developed from now on. Consequently, there will be increased necessity to cope with the pattern-effects in medium current ion implantation machines that have not experienced these problems up to now.

Chapter 5. Conclusion

The high controllability and reproducibility of ion implantation technology has formed the basis for the continued progress toward miniaturization and higher performance of Si semiconductor devices. To control the manufacturing variations for the next generation semiconductor devices with successively greater miniaturization and higher performance requires analysis and control of the damage produced in the semiconductor material by the ion irradiation. The manufacturing variations are a difficult problem issued in mass production factories but not at the research laboratories. The techniques to evaluate the semiconductor material damage by ion irradiation have then been examined in the present work, to develop analysis technologies which can be used in-line, or will possibly be available in the future. The conclusions are summarized as follows:

(1) The thickness of the amorphized layer formed on the Si substrate by ion implantation, was measured using the spectroscopic ellipsometry (SE), and the quality of the amorphous-crystalline boundary was evaluated. Comparison of the amorphized layer thicknesses measured by the SE, the HR-RBS and the X-TEM showed that the layer thickness by the SE extends to the high-damage region of the amorphous-crystalline boundary transition region. In addition, this region is extremely sensitive to its thermal history, and it has been found that the activation energy for the recovery of crystallinity of the amorphized layer is 0.17 eV, which is an order of magnitude lower than the activation energy perceived for usual implantation damage.

By utilizing this sensitivity of the boundary layer to thermal history, it is possible to evaluate the implantation beam characteristics. The relationship between the ion

beam parameters and the amorphized layer thickness was then examined. These results showed that the amorphized layer thickness increases with the ion beam current within the region of the boundary, and depends also on the implantation dose and the ion energy. It was also found, from comparison with the concentration of recoil Si atoms calculated with a Monte Carlo simulation code, SRIM, that the critical density above which the layer is regarded as the amorphized layer is 1×10^{22} cm^{-3}.

The SE finds frequent use as a thickness gauge for, e.g., SiO_2, in semiconductor production processes. In this respect, it is expected that the findings of the present study could be indispensible not only for the development of semiconductor devices, but also for an in-line method of evaluating the ion implanter characteristics in semiconductor plants.

(2) The grazing-angle incidence PIXE method was successfully applied as a method to evaluate the cross-contamination. The lower limit for detection of impurities in the Si substrate has been around 1×10^{14} cm^{-2} with use of the conventional PIXE method. By implementing grazing-angle incidence the detection limit is lowered in proportion to $1/\cos\theta$. Consequently, the lower limit for detection was successfully reduced to 1×10^{13} cm^{-2}. This inevitably increases signals of the background X rays due to bremsstrahlung from the Si substrate also increasing in proportion to $1/\cos\theta$. So, attention was focused on the photo-resist, which is used almost without exception as a mask during ion implantation. With the grazing angle-incidence the relative decrease in the bremsstrahlung background can be expected since the emission rate is independent of the incident angle. The resulting lower limit for detection of impurities was lowered successfully to 1×10^{12} cm^{-2}. This means that the control of a cross-contamination of approximately 1 % could be possible.

Then, the amount of cross-contamination in a batch-type high-current ion implanter was measured. The result was that the cross-contamination of the order of 1 % can be detected. It was also found that cleaning by Ar beam irradiation can not lead to any significant reduction in the cross-contamination.

Given the recent trend toward compact accelerators, in-line use of grazing-angle-incidence PIXE is a real possibility in the near future.

(3) An evaluation of the charging phenomenon, which happens during irradiation of the photo-resist surface, was performed with the aid of a surface potential measurement tool. A carbonized layer due to the ion implantation began to be formed on the photo-resist surface even in the dose range of 1×10^{13} cm^{-2}. This layer is formed because the photo-resist molecules are broken down by the impact of the implanted ions to release hydrogen atoms, which results in hydrogen gas emission and cross-linking reactions of the carbon-rich residues. The layer is formed more easily for the photo-resist having a molecular structure with low binding energy. Through the carbonized layer with a low resistance on the photo-resist surface, the accumulated charge introduced on the photo-resist by the implanted ions flows into the aperture. This inflow of the charge into the aperture causes severe problems such as the explosion-like discharge issue even in the medium-current implanters.

Compared to the i-line photo-resist, this phenomenon is more prominent in acetal KrF photo-resist, whose molecule has a minimum binding energy even lower than the former, and would occur even for a dose less than 1×10^{13} cm^{-2}. From now on, both improvement of photo-resist material which accompanies the continued trend of miniaturization of devices, and the diversification of aperture ratios which accompanies continued leveling up of the system LSI, is considered to increase the risk of occurrence

of the charging phenomenon in medium-current ion implantation.

In summary, the techniques to evaluate semiconductor material damage by ion irradiation were developed using analysis techniques which can be used in-line in semiconductor manufacturing facilities, or will possibly be available in the future. This made it possible to clarify some of the main factors causing manufacturing variations in ion implantation which had been previously unclear.

In the future, in response to the likely further advances in the digitalization in the society, semiconductor devices become more and more important. For semiconductors, playing the most important role in the intellectual part of the infrastructure of the society, besides the requirements of small size and high performance, “stability” needs to be pursued as a top priority. The evaluation techniques developed in the present study, and the clarification of the mechanism for ion irradiation damage in semiconductor materials which has been obtained by means of these techniques, will surely contribute to the stability of characteristics of the semiconductor components that forms the basis for stability of the semiconductor devices as a whole.

The ion irradiation damages in semiconductor materials whose mechanisms have been revealed in the present study are only in a small part of the phenomena. An important point for the further development in stability of semiconductor devices is the further effort toward verification of the effect of ion irradiation on a myriad of new semiconductor materials developed in the future.

ACKNOWLEDGMENTS

I would like to express sincere gratitude to Professor Akira Kitamura of the Graduate School of Maritime Sciences, Kobe University, for his continuing guidance, precise advice, and encouragement during this work.

I would like to acknowledge Dr. Micheal Current for his valuable comments and discussions. I also would like to acknowledge Dr. Genshu Fuse, SEN Corporation, and Dr. Woo Sik Yoo, WeferMasters, Inc., for their valuable comments and discussions.

I would like to thank Mr. Fumitoshi Kawase, Ms. Yuko Nambu, and Ms. Emi Kanazaki, semiconductor Company Panasonic Corporation, for their help in the experiments. I also thank Ms. Hisako Kamiyanagi, Mr. Reiki Kaneki, Mr. Akihiko Kitada, Panasonic Semiconductor Engineering Co., Ltd., for their cooperation in the experiments.

I would like to thank all members of SEN Corp., NISSIN ION EQUIPMENT Co., Ltd., The Kobelco Research Institute, KLA-Tencor Corp., WeferMasters, Inc., and Axcelis Technologies, Inc. for their support of my experiments.

I would like to thank Mr. Hideo Niko, president of Panasonic Semiconductor Opto Devices Co., Ltd. Mr. Hirofumi Fukumoto, former general manager of Panasonic Tonami plant. Mr. Daihei Kajiwara, plant superintendent of Panasonic Arai plant, Mr. Hiroyuki Kuroda, plant superintendent of Panasonic Uozu plant, Mr. Katsuyuki Ikenouchi, plant superintendent of Panasonic Tonami plant and Hiroyuki Kawahara, manager of Panasonic Tonami plant. They gave me the opportunity to perform this work, and encouraged warmly.

I also thank Mr. Hidetsugu Asada, Director of Materials Science and Analysis Technology Center (MSAC), Panasonic Corp., Ms. Emiko Igaki, general manager of

MSAC, Mr. Yoshiaki Tsukamoto, manager of MSAC, Mr. Hiromi Morita, chief engineer of MSAC, Mr. Tetsuyuki Okano, Mr. Takashi Kouzaki, Ms. Miori Hiraiwa, Ms. Tomoko Kawashima, and Mr. Akihiko Sagara, MSAC, for their support.

Finally I thank my wife Yuko Shibata for her constant encouragement.

REFERENCES

[1] "The Process Integration, Devices, and Struc-tures " ITRS 2009 Edition PP. 3-4.

[2] W Shockley, U. S. Patent No. 2, 787, 564(1957).

[3] Peter H. Rose "Ion implantation, yesterday and today" SOLID STATE TECHNOLOGY, Vol. 40, No. 40-5, (1997), PP. 129-130.

[4] J. F. Ziegler, "The History of Integrated Circuits and Ion Implantation ", in Ion Implantation Science and Technology, 2010 Edition, edited by J.F. Ziegler, Ion Implantation Technology Press (2010), PP. 1-22.

[5] K. Ynoeda, M. Niwayama, "The drain current asymmetry of 130 nm MOSFETs due to extension implant shadowing originated by mechanical angle error in high current implanter" IEEE Proc. Junction Technology, IWJT2002, (2002), PP. 19-22.

[6] Y, Kawasaki, K. Tokunaga, K. Horita, K.Mitsuda, A.Yamaguchi, A. Ueno, A. Teratani, T. Katayama, K. Hayami, A.Togawa, Y. Ohno, and M. Yoneda, "The collapse of gate electrode in high-current implanter of batch type" IEEE Proc. Junction Technology, IWJT2004 (2004), PP. 39-41.

[7] M. Schmeide, S. Kontratenko, R. P. Mu¨ller, and B. Krimbacher, "Integration of an Axcelis Optima HD Single Wafer High Current Implanter for p- and n-SOD Implants in an Existing Batch Implanter Production Line" A.I.P. Proc. 1066, 17th International Conference on Ion Implantation Technology, IIT08" (2008), PP. 332-335.

[8] M. Sugitani, M. Tsukihara, M. Kabasawa, K. Ishikawa, H. Murooka, and K. Ueno, "Introduction of the SHX-III System, a Single-Wafer High-Current Ion Implanter" A.I.P. Proc. 1066, 17th International Conference on Ion Implantation Technology, IIT08" (2008), PP. 292-295.

[9] O. F. Campbell, A. M. Ray, M. Sugitani, and F. Sato, "Introducing the MC3 Medium Current 300 mm Implanter" IEEE. Proc. 14th International Conference on Ion Implantation Technology, IIT02" (2002), PP. 292-295.

[10] M. Tanjyo, S. Sakai, T. Ikejiri, K. Tanaka, Y. Koga, T. Kobayashi, T. Matsumoto, M. Nakaya, Y. Kibi, T. Yamashita, T. Nagayama N. Hamamoto, S. Umisedo, S. Yuasa, M. Naito, and N. Nagai, "High quality ion implanter; EXCEED3000AH-Nx for 45nm beyond I/I process<Beam Size and Angle>" IEEE Proc. Junction Technology, IWJT2006, (2006), PP. 31-35.

[11] Y. Tamura, M. Nogami, M. Tanaka, T. Maeda, H. Kumasaki and S. Tamura, "Production Implanter Nissin NH-20SR" Nuclear Instruments and Methods in Phisics Research B 37/38 (1989), PP. 620-623.

[12] N. R. White, N. Tokoro, and E. Bell "Radiation Issues Surrounding Very High Energy Ion Implantation" A.I.P. Proc. 1066, 17th International Conference on Ion Implantation Technology, IIT08" (2008), PP.277-280.

[13] N. Suetsugu, M. Tsukihara, K. Ueno and M. Sugitani, "Demand for Image Sensor Devices on High Energy Implantation and Solution with the UHE, an Higher Energy Implanter" Presentation on 18th International Conference on Ion Implantation Technology, IIT10, 7-11 Jun. (2010), Kyoto.

[14] S. Chang, V. Chavva, F. Sinclair, "True Zero Implants" Presentation on 18th International Conference on Ion Implantation Technology, IIT10, 7-11 Jun. (2010), Kyoto.

[15] S. Satoh, J. Ferrara, E. Bell, S. Patel, and M. Sieradzki, "Optima XE Single Wafer High Energy Ion Implanter" A.I.P. Proc. 1066, 17th International Conference on Ion Implantation Technology, IIT08" (2008), PP.273-276.

[16] L. Pelaz, L. A. Marqués, and J. Barbolla, "Ion-beam-induced amorphization and recrystallization in silicon" J. Appl. Phys. 96, 5947 (2004) PP. 30.

[17] N. Hamamoto., S. Umisedo, T. Nagayama, M. Tanjyo, S. Sakai, N. Nagai, T. Aoyama , and Y. Nara, "Decaborane implantation with the medium current implanter" Nuclear Instruments and Methods in Physics Research B 237 (2005), PP. 443–448.

[18] Y. Kawasaki, T. Kuroi, T. Yamashita, K. Horita, T. Hayashi, M. Ishibashi, M. Togawa, Y. Ohno, M. Yoneda, T. Horsky, D. Jacobson, W. Krull, "Ultra-shallow junction formation by $B_{18}H_{22}$ ion implantation" Nuclear Instruments and Methods in Physics Research B 237 (2005), 25–29.

[19] K. Kugimiya, G. Fuse, "Blink Furnace Annealing of Ion-Implanted Silicon" J. J. Appl. Phys. Vol. 21, No. 1, (1982), PP. L16-L18.

[20] J. Hebb, A. Shjii, and M.Flynn, "Furnace-based rapid thermal processing" SOLID STATE TECHNOLOGY, Vol. 43, No. 10, (2000), PP. 155.

[21] M. Ameen, J. Hebb, "Implanter, RTP system issues for ultrashallow junction formation" SOLID STATE TECHNOLOGY, Vol. 44, No. 9, (2001), PP. 77.

[22] Y. Wang, S. Chen, M. Shen, X. Wang, S. Zhou, J. Hebb, D. Owen, "Dual Beam Laser Spike Annealing Technology" IEEE Proc. Junction Technology, IWJT2010, (2010), PP. 18-23.

[23] H. Kiyama, S. Kato, T. Aoyama, T. Onizawa1, K. Ikeda, H. Kondo, K. Hashimoto, H. Murakawa, T. Kuroiwa "Advanced Flash Lamp Annealing technology for 22nm and further device" IEEE Proc. Junction Technology, IWJT2010, (2010), PP. 24-29.

[24] S. N inomiya, Y. Kimura, T. Kudo, A. Ochi, F. Sato, M. Tsukihara, G. Fuse, M. Sugitani, K. Tada, H. Kamiyanagi, Satoshi Shibata, "Vth control by halo

implantation using the SEN's MIND system" IEEE. Proc. The 9th International Workshop on Junction Technology 2009, (2009), PP.100-103.

[25] F. Kawase, H. Kmiyanagi, E. Kanazaki, and S. Shibata, "Development of gate length feed-forward technology for controlling variability of Vtp" Abstract. AEC / APC Symposium Asia 2009, (2009).

[26] E. Kanazaki, N. Iwawaki, F. Kawase, and S. Shibata, "Implant Damage Evaluation at High Energy and Low Dose Ion Implantationusing White Defect of CCD Image Sensor" IEEE. Proc. The 9th International Workshop on Junction Technology 2009, (2009), PP106-109.

[27] T. F. Kelly, and M. K. Miller, "Atom probe tomography" Rev. Sci. Instrum. 78, 031101 (2007).

[28] L. Zhang, M. Saitoh, M. Koike and S. Takeno, H. Tanimoto1, K. Adachi1, N.Yasutake1, and N. Kusunoki, "High-resolution and Site-specific SSRM on S/D Engineering" IEEE Proc. Junction Technology, IWJT2010, (2010).

[29] K. S. Jones, K. Moller, J. Chen, M. Puga-Lambers, M. Law, D. S. Simons, P. Chi, B. Freer, J. Bernstein, L. Rubin, R. Simonton, R. G. Elliman, M. Petravic, and P. Kringhoj, "The effect of end of range loops on transient enhanced diffusion in Si" *IEEE Proc. 11th International Conference on Ion Implantation Technology, IIT96,* 96TH8182, (1996), PP. 618-621.

[30] K. S. Jones, V. Krishnamoorthy, L. H. Zhang, M. Law, D. S. Simons, P. H. Chi, L. Lubin, and R. G. Elliman, "Using doping superlattices to study transient-enhanced diffusion of boron in regrown silicon" Appl. Phys. Lett., 68, (1996), PP. 3111-3113,.

[31] N. E. Cowern "Source-Drain Engineering for Channel-Limited PMOS Device Performance: Advances in Understanding of Amorphization-Based Implant Techniques" *Proc. Mater. Res. Soc. Symp.* 1070, (2008), PP. 143-154.

[32] M.I. Current, S. Felch, T. Kuroi, A. Jain, P. Timans, D. Jacobson, and J. Hautala, in *Ion Implantation Science and Technology*, 2008 Edition, edited by J.F. Ziegler, Ion Implantation Technology Press (2008).

[33] K.S. Jones, L. Romano, N.G. Rudanski, J. Gyulai, and P. Petrik, in Ion Implantation Science and Technology, 2008 Edition, edited by J.F. Ziegler, Ion Implantation Technology Press, 2008.

[34] K. Okabe, R. Miura, and M. Kase, "65nm Device Characteristics Matching on Single and Batch System Ion Implanter" A.I.P. Proc. 16th International Conference on Ion Implantation Technology, IIT06, CP866, (2006), PP. 645-648.

[35] M.S. Ameen, M.A. Harris, C. Huynh, and R.N. Reece, "Damage Rate Effects: The Impact of Beam Dynamics on Materials Issues and Device Performance" A.I.P. Proc.

17th International Conference on Ion Implantation Technology, IIT08, CP1066, (2008), PP. 30-33.

[36] G. Fuse, M. Sano, H. Murooka, T. Yagita, M. Kabasawa, T. siraishi, Y. Fujino, N. Suetsugu, H. Kariya, H. Izutani, M. Sugitani," Electrical characteristics due to differences in crystal damage induced by various implant conditions" Nucl. Instrum. Methods Phys.Res., Sect. B 237, (2005), PP. 77-82.

[37] S. Shibata, Y. Nambu, R. Etou, and G Fuse, " Evaluation of high dose ion implantation by spectroscopic ellipsometry" IEEE Proc. 12th Int. Conf. on Ion Implantation Technology. 1998, 98X144 (1999), PP. 465-467.

[38] S. Shibata, Y. Nambu, H. Izutani , T. Morita, K. Yamazawa, and M. Arai, "Real Exposed Temperature Evaluation UsingReordering of Implanted Amorphous Si Layers" IEEE Proc. Int. Symposium on Semiconductor Manufacturing 2003, (2003), PP. 339 – 342.

[39] Y. Nambu, S. Shibata, K. Itonaga, S. Hashimoto, and G Fuse, "Reordering of Implanted Amorphous Si Layers with Low Temperature RTA IEEE Proc. 12th Int. Conf. on Ion Implantation Technology1998. 98X144, (1999), PP. 642-645,.

[40] K. Yamazawa, M. Arai, S. Shibata, Y. Nambu, H. Izutani, and T. Morita, "A wafer surface temperature measurement method utilizing the reordering phenomena of amorphous silicon" IEEE Proc. SICE-ICASE International Joint Conference 2006. (2006), PP. 3351 – 3355.

[41] Y. Sasaki, C. G. Jin, H. Tamura, B. Mizuno, R. Higaki, T. Satoh, K. Majima, H. Sauddin, K. Takagi, S. Ohmi, K. Tsutsui, and H. Iwai "B_2H_6 plasma doping with "in-situ He pre-amorphization" Proc. Symposia on VLSI Technology 2004, (2004), PP. 180-181.

[42] Y. Sasaki, C. G. Jin, K. Okashita, H. Tamura, H. Ito, B. Mizuno,H. Sauddin, R. Higaki, T. Sato, K. Majima, Y. Fukagawa, K. Takagi, I. Aiba, S. Ohmi, K. Tsutsui, and H. Iwai, "New method of Plasma doping with in-situ Helium pre-amorphization" Nuclear Instruments and Methods in Physics Reseach B237, (2005), PP.41-45.

[43] Y. Hori, AIST Bulletin of Metrology. Tech. Rep.Vol. 6, (2007), PP.16 [in Japanese].

[44] H. Fuziwara, Bunkoueripusometori (Spectroscopic ellipsometry) (Maruzen, Tokyo, (2003), PP.117 [in Japanese].

[45] K. Kimura, Y. Mori, M. Maehara, and Fukuyama, "Development of Compact High-Resolution RBS System for Monolayer Analysis" Proc. CP475, Applications of Accelerators in Research and Industry 1999, (1999), PP.500-503..

[46] G. E. Jellison, Jr. and F. A. Modine, "Parameterization of the optical functions of amorphous materialsin the interband region" Appl. Phys. Lett. 69 (3) (1996), PP. 371.

[47] F. Wooten, Optical Properties of Solids, Academic Press, New York, (1972), PP.42.

[48] L. Ward, The Optical Constants of Bulk Materials and Films, Adam Hilger, Philadelphia, (1988), PP.14.

[49] J. Shin Chen, S. Chao, J. Shium, Kao H. Niw, and C. Hsin Chen, "Mixed films of TiO_2—SiO_2 deposited by double electron-beam coevaporation" Appl. Opt. 35, 90, (1996).

[50] H. Piller, Handbook of Optical Constants of Solids I, edited by E. D.Palik , Academic Press, New York, (1985), PP. 571.

[51] J. F. Ziegler, http://www.srim.org/index.htm#HOMETOP.

[52] W. S. Yoo, T. Fukada, H. Kuribayashi, H. Kitayama, N. Takahashi, K. Enjoji, and K. Sunohara, "Slip-Free Rapid Thermal Processing in Single Wafer Furnace" Jpn. J. Appl. Phys. 39, Part 1, No. 11, (2000).

[53] W. S. Yoo, T. Fukada, H. Kuribayashi, H. Kitayama, N. Takahashi, K. Enjoji, and K. Sunohara, "Single Wafer Furnace and Its Thermal Processing Applications" Jpn. J. Appl. Phys. 39, Part 2, No. 7A, (2000).

[54] L. Csepregi, E. F. Kennedy, T. J. Gallagher, J. W. Mayer, and T. W. Sigmon, "Reordering of amorphous layers of Si implanted with ^{31}P, ^{75}As, and ^{11}B ions" J. Appl. Phys. 48, 10, (1977), PP. 4234-4240

[55] J. A. Roth, G. L. Olsen, D.C. Jacobson, and J. M. Poate, "Kinetics of solid phase epitaxy in thick amorphous Si layers formed by MeV ion implantation" Appl. Phys. Lett. 57 (13), (1990), PP. 1340-1342.

[56] TF. Tachibana and T. Hiramoto, "Re-examination of Impact of Intrinsic Dopant Fluctuations on SRAM Static Noise Margin", Japanese Journal of Applied Physics, Vol. 44, Part 1, No. 4B, (2005), PP. 2147 – 2151.

[57] H. Ryssel, M.I. Current, and L. Frey, "Contamination Control for Ion Implantation", in Ion Implantation Science and Technology, 2004 Edition, edited by J.F. Ziegler, Ion Implantation Technology Press (2004).

[58] L. A. Larson and M. I. Current, "Metallic impurities and dopant cross-contamination effects in ion implanted surfaces" MRS Symposia Proc. Of the Ion Beam Processes in advanced Electronic Materials and Device Technology, (1985), PP. 381-388.

[59] M.I. Current, P. Eyben, P. Nielsen, M. Benjamin, E. Tsidilkovski, A. Salnik, A. Buczkowski, T. Kelly and N. Ikarashi, "New Metrology Methods for Ion Implantation Process Controls", in Ion Implantation Science and Technology, 2008 Edition, edited by J.F. Ziegler, Ion Implantation Technology Press (2008).

[60] J. Halim, A. Mineji, V. Faifer, and M. I. Current, "High-Resolution Mapping of Low-Dose Implants". A.I.P. Proc. of the 17th International Conference on Ion Implantation Technology 2008. Volume 1066, (2008), PP. 175 – 178.

[61] F.A. Stevie, R.G.Wilson, D.S. Simons, M.I. Current, and P.C. Zahm, "Review of secondary ion mass spectrometry characterization of contamination associated with ion implantation" J. Vac. Sci. Tech. B,12 (4) (1994), PP. 2263-2279.

[62] P.F. Staub, C. Hombourger, and M. Schuhmacher, Quantitative determination of dopant dose in shallow implants using the low energy x-ray emission spectroscopy technique J. Vac. Sci. Tech. B, 20 (1), (2002), PP. 436-440.

[63] S. F. Corcoran, C. Hombourger, P.F. Staub, and M. Schuhmacher, "High Accuracy and Rapid Dose Measurements for Ultra-Low Energy Ion Implantation using Low Energy X-ray Emission Spectroscopy" IEEE Proc. of the 14th International Conference on Ion Implantation Technology , Issue , (2002), PP. 165 - 168.

[64] R. Klockenkaemper, M. Becker, H. Bubert, P. Burba, and L. Palmetshofer, "Determination of the implantation dose in silicon wafers by X-ray fluorescence analysis" Anal. Chem., 62 (15), (1990), PP. 1674–1676.

[65] Y. Mori, K. Uemura "Bunnseki-Kagaku" Vor. 53, (2004), PP. 61, [in Japanese].

[66] S. A. E. Jonshansson, J. L. Campbell, and K. G. Malmqvist, Particle induced X-ray emission (PIXE), Chemical Analysis Series, Vol133, John Wiley & Sons, Inc. (1995), New York.

[67] A. Kitamura, Y. Furuyama, A. Taniike, and N. Kubota, Review of Kobe University of Mercantile Marine, 46 (1998) 1 [in Japanese].

[68] J. L. Campbell : http://pixe.physics.uoguelph.ca/home/.

[69] J. F. Ziegler, http://www.srim.org/index.htm.

[70] S. Yedave, J. Sweeney, O. Byl, S. Letaj, M. Wodjenski, M. Hilgarth, P. Marganski, S. Bishop, D. Eldridge, and R. Kaim "Development of "Static" In-Situ Implanter Chamber Cleaning" AIP Conf. Proc. Of 17th International Conference on Ion Implantation Technology; issue, (2008), PP. 376-379.

[71] M. S. Ameen, M.E. Mack, "Wafer Cooling and Wafer Charging", in Ion Implantation Science and Technology, 2004 Edition, edited by J.F. Ziegler, Ion Implantation Technology Press (2004).

[72] M.I. Current, M. A. Foad, S. Brown, W. Lukaszek, and M. C. Vella, "Photoresist Effects on Wafer Charging Control: Current-voltage Characteristics Measured with CHARM-2 Monitors during High-current As+ Implantation" , IEEE Proc. 12th Int. Conf. on Ion Implantation Technology. 1998, 98X144, (1999), PP. 490-493.

[73] M.I. Current, W. Lucaszek, M.C Vella, "Control of Wafer Charging during Ion Implantation: Issues, Monitors and Models", Proc. Of 5th Inter. Symp. on Plasma Process-induced Damage, P2ID-2000, AVS, IEEE, Japan Soc. of Applied Physics, (2000), PP. 137-140.

[74] N. Aoki, K. Ishikawa, T. Namura, Y. Fukuzaki, G. Fuse, M. Yoshida and M. Inoue "Evaluation of ion implantation charging by using EEPROM" Nuclear Instruments and Methods in Physics Research Section B: Beam Interactions with Materials and Atoms Volume 74, Issues 1-2, (1993), PP. 306-310.

[75] H. Kubo, T. Namura, Kenji Yoneda, H. Ohishi, and Y. Todokoro, "Quantitative Charge Build-Up Evaluation Technique by Using MOS Capacitors with Charge Collecting Electrodes in Wafer Processing" IEICE TRANS. ELECTRON., VOL. E79 C. NO. 2 (1996).

[76] P. F. Kurunczi, A. S. Perel, E. Wright, S. Kikuchi, and J. T. Scheuer "Advanced Charge Control for Single Wafer Implanters" A.I.P. Proc. 16th International Conference on Ion Implantation Technology, IIT06, CP866, (2006), PP. 445-448,.

[77] S. Fujimura, H. Yano and J. Konno "Ion implantation change in the chemical structure of a resist" Nuclear Instruments and Methods in Physics Research Section B: Volume 39, Issues 1-4, (1989), PP. 809-812.

[78] S. Fujimura, J. Konno, K. Hikazutani and H. Yano "Ashing of Ion-Implanted Resist Layer" Jpn. J. Appl. Phys. 28, (1989), PP. 2130-2136.

[79] T. Sanada, M. Watanabe, A. Hayashida, and Y. Isago "Post Ion-Implant Photoresist Stripping Using Steam and Water: Pre-treatment in a steam atmosphere and steam-water mixed spray" Solid State Phenomena Vols. 145-146 (2009), PP. 273-276.

[80] M. Yamamoto, T. Maruoka, Y. Goto, A. Kono, H. Horibe, M. Sakamoto, E. Kusano, H. Seki, and S. Tagawa, "Removal of Ion-Implanted Photoresists Using Atomic Hydrogen" Journal of The Electrochemical Society, 157 , 3, (2010), PP. H361-H370 .

[81] K. L. Chavez, G. L. Bakker, D. W. Hess "Ion-implanted photoresist removal using water/carbon dioxide mixtures at elevated temperature and pressure" J. Vac. Sci. Technol. B 19.6., (2001), PP.2144-2148.

[82] J. C. Vickerman " ToF-SIMS- An Overview" in ToF-SIMS edited by J. C. Vickerman and D. Briggs, IM Publications and Surface Spectra Limited, UK. (2001), PP.1-40.

[83] N. Nagai, I. Nishiyama, Y. Kishima, K. Iida, and K. Mori "Infrared Surface Analysis Using a Newly Developed Thin-Sample Preparation System" APPLIED SPECTROSCOPY Volume 63, (2009), PP. 66-72.

[84] http://www.trekinc.com/products/541A.asp.

[85] J. F. Ziegler, http://www.srim.org/index.htm#HOMETOP.

[86] “Kagaku Binran” [in Japanese] edited by The Chemical Society of Japan , Maruzen Co. Ltd., (1993), Basic-2-PP.301.

List of Publications

Journal full papers

Chapter 2

1) Satoshi Shibata, Fumitoshi Kawase, Akihiko Kitada, Takashi Kouzaki, and Akira Kitamura, "Evaluation of Pre-Amorphized Layer Thickness and Interface Quality of High-Dose Shallow Implanted Silicon by Spectroscopic Ellipsometry" IEEE TRANSACTIONS ON SEMICONDUCTOR MANUFACTURING, VOL. 23, NO. 4, NOV. 2010 PP. 545 – 552.

Chapter 3

2) Satoshi Shibata, Hisako Kamiyanagi, Tetsuyuki Okano, and Akira Kitamura, "New Evaluation Method for cross-contamination of ion implantation by using a grazing angle incidence PIXE in Photo-resist." IEEE TRANSACTIONS ON SEMICONDUCTOR MANUFACTURING, VOL. 23, NO. 3, AUGUST 2010, PP. 423 – 428.

Chapter 4

3) Satoshi Shibata , Hisako Kamiyanagi, Fumitoshi Kawase, Reiki Kaneki, Tomoko Kawashima and Akira Kitamura, "Charging phenomena during medium current ion implantation of carbonized photo-resist surface layers" to be published in IEEE TRANSACTIONS ON SEMICONDUCTOR MANUFACTURING, VOL. 24.

International conference Proceedings

Chapter 1

1) Emi Kanazaki, Naoki Iwawaki, Fumitoshi Kawase, and Satoshi Shibata, "Implant Damage Evaluation at High Energy and Low Dose Ion Implantationusing White Defect of CCD Image Sensor" IEEE. Proc. The 9th International Workshop on Junction Technology 2009, (2009) PP.106-109.
2) S. Ninomiya, Y. Kimura, T. Kudo, A. Ochi, F. Sato, M. Tsukihara, G. Fuse, M. Sugitani, K. Tada, H. Kamiyanagi, Satoshi Shibata, "Vth control by halo implantation using the SEN's MIND system" IEEE. Proc. The 9th International Workshop on Junction Technology 2009, (2009) PP. 100-103.

Chapter 2

3) Satoshi Shibata, Yuko Nambu, Ruichi Etou, and Genshu Fuse, " Evaluation of high dose ion implantation by spectroscopic ellipsometry" IEEE Proc. 12th Int. Conf. on Ion Implantation Technology. 1998, (1998) PP. 465-467.
4) Yuko Nambu, Satoshi Shibata, Kazuichirou Itonaga, Shin Hashimoto, and Genshu Fuse, "Reordering of Implanted Amorphous Si Layers with Low Temperature RTA" IEEE Proc. 12th Int. Conf. on Ion Implantation Technology1998. (1999), PP. 642-645.
5) Satoshi Shibata, Yuko Nambu, Hsaki Izutani , Takeo Morita, Kazuaki Yamazawa, and Msaru

Arai, “Real Exposed Temperature Evaluation UsingReordering of Implanted Amorphous Si Layers” IEEE Proc. Int. Symposium on Semiconductor Manufacturing 2003, (2003), PP. 339 – 342.

6) Kazuaki Yamazawa, Masaru Arai, Satoshi Shibata, Yuko Nambu, Hisaki Izutani, and Takeo Morita, “A wafer surface temperature measurement method utilizing the reordering phenomena of amorphous silicon” IEEE Proc. SICE-ICASE International Joint Conference 2006” (2006). PP. 3351 – 3355.

7) Satoshi Shibata, Fimitoshi Kawase, Aakihiko Kitada, Takashi Kouzaki “Evaluation of Pre-amorphous Layers by Spectroscopic Ellipsometry” A.I.P. Proc. 1066, 17th International Conference on Ion Implantation Technology, IIT08” (2008), PP. 190-193.

8) Satoshi Shibata, Fumitoshi Kawase, Akio Kitada, Takashi Kouzaki Akira Kitamura, Kazuaki Yamazawa, Masaru Arai, Yuko Nambu, Hisaki Izutani, and Takeo Morita, “Evaluation by Spectroscopic Ellipsometryof Si amorphized layer thickness after implantation and solid phase re-growth at low annealing temperatures” IEEE Proc. The 10th International Workshop on Junction Technology, (2010), PP. 90-94.

Chapter 4

9) Hisako Kamiyanagi, Satoshi Shibata “Charging phenomena of the medium dose implantation by a carbonization of the surface layer of the photo-resist” IEEE. Proc. The 5th International Workshop on Junction Technology 2005, (2005), PP. 65 – 68.